CHLORIDE PITTING CORROSION OF API X-80 and X-100 HIGH STRENGTH LOW ALLOY PIPELINE STEELS IN BICARBONATE SOLUTIONS

by

MASLAT S. ALWARANBI

B.Sc., King Fahd University of Petroleum and Minerals, 1999

A THESIS SUBMITTED IN PARTIAL FULFILLMENT OF
THE REQUIRMENTS FOR THE DEGREE OF

MASTER OF APPLIED SCIENCE

in

THE FACULTY OF GRADUATE STUDIES

(Materials Engineering)

THE UNIVERSITY OF BRITISH COLUMBIA

December 2006

ABSTRACT

The corrosion polarization behaviors of API X-80 (550 Grade) and API X-100 (690 Grade) pipeline steels in bicarbonate/chloride media were investigated by means of electrochemical techniques. In bicarbonate free chloride containing solutions, both steels revealed practically similar polarization behaviors exhibiting active/passive transitions with a varying number of distinct oxidation peaks. The bicarbonate concentration increase in the solutions was found to expand the passive potential region and result in more noble breakdown potentials. In contrast, the addition of small amounts of chloride ions evidently influenced the shape of the polarization curves where the corrosion rates were increased, the passive potential regions were narrowed in width, and the pitting potentials were shifted in the negative direction.

The corrosion characteristics under the same prevailing experimental conditions of both steels indicated that API X-100 steel grade had lower corrosion rates in all tested bicarbonate solutions with and without the presence of chloride ions and better pitting corrosion resistance for the range of chloride concentrations investigated. This may have been attributed to the higher alloying content of molybdenum, nickel and copper in API X-100 steel over API X-80 grade and accordingly in the variance of the final microstructure formed for both steels which in turn could have made a change in the thickness and the protectiveness of the passive layers formed on the surfaces of the steels.

Pitting morphology features such as the average diameter and density of active pits were examined by the Scanning Electron Microscopy (SEM). SEM observations showed that solutions of low bicarbonate concentrations (0.01 and 0.05M) resulted in a comparatively bigger size of pits, while solutions of higher bicarbonate concentrations (0.1 and 0.5M) showed no pits. This major difference may be due to the more stable passive films produced on the steel surfaces having higher bicarbonate concentrations. On the other hand, pit morphology as examined by the SEM technique for the bicarbonate solutions consisting of different concentrations of chloride ions indicated that the density and the average diameter of the stable corrosion pits increased with increasing the chloride concentrations in the test solutions.

TABLE OF CONTENTS

LIST OF TABLES

LIST OF FIGURES

ACKNOWLEDGEMENTS

First, I would like to express my sincerest gratitude to my supervisor, Professor Akram Alfantazi for his guidance and encouragement throughout the whole course of this project. This thesis would not have been achievable without the persistent support, kindness, patience and care he afforded me. I also would like to thank the examining committee members, Professors S. Cockcroft, Elod Gyenge, Rizhi Wang and Joseph Kish for stimulating valuable discussions and comments on the thesis.

My heartfelt acknowledgement extends to my sponsoring company, Saudi Arabian Oil Company (Saudi Aramco) for the scholarship endowment it granted me along the course of work. I also would like to offer my genuine thanks to my Career Development Department advisor, Ted Kalivoda, my CSD/CTU mentor Ivan Cruz and CTU supervisors for their continuous follow up and assistance they provided to help resolve any outstanding issue that may stop me from accomplishing this mission. I am also deeply thankful to Materials Technology Laboratory (MTL), CANMET for supplying the materials required to undertake this project. I am also indebted to my colleagues, Tawfik Ahmed, Edward Asselin, Ali Abugussah and James Vaughan for their dedication in providing a helping hand, experimental assistance and fruitful discussions throughout this work.

Finally, I am eternally appreciative to my wife for her patience and understanding, to my father and mother for their daily prayers, and to all my family and friends for their continual support and encouragement.

CHAPTER ONE

1 Introduction

Pipelines are one of the most convenient means of transporting natural gas and crude oil from production sites to the consumer. They are efficient, economic and can last for several decades. In common, High Strength Low Alloy (HSLA) steels, also known as micro-alloyed steels, have been recognized as the mostly utilized steels for pipeline construction in the petroleum industry. These steels have been evolved in order to attain the required mechanical properties and fulfill the diameter and thickness designs of such pipelines [1]. To obtain the former characteristics, steel makers produce these steels with a wide range of microstructures and chemical compositions developed by various manufacturing processes. The American Petroleum Institute (API) classifies pipeline steels used in hydrocarbon production and transport environments as API 5LX steels [2].

Much of the existing infrastructure has made use of pipe grades up to API X-70 (483 MPa) steel [3]. For the pipeline infrastructure in Western Europe and North America, the most recent evolutionary step has been grade API X-80 (550 MPa) steel [3]. After a 20 year development period, this is now established as a fully satisfactory material technology for constructing pipelines up to 1200 mm diameter operating at up to around 100 bar.

In recent years, oil and gas companies have shown an increasing interest in the possible use of higher grade steel pipes such as API X-100 (690 MPa) steel grade and higher for constructing the future long distance pipelines [4,5,6,7]. The use of a high strength grade offers potential benefits with respect to using a higher operating pressure without increasing the pipe wall thickness. This in turn offers economic benefits arising from lower material, transportation and fabrication costs.

Modern grade API X-100, first produced in trials nearly 10 years ago, has been evaluated and many of the issues connected with the manufacture, design, construction and operational performance have been now addressed, adding confidence to the acceptability of API X-100 pipeline steel for future highly rated applications. More recently, for the first time TransCanada installed and welded the highest grade pipeline steel available in the world today, X-120 (825 MPa) grade and steps are under way to address the same issues for this material [8].

As with any other engineering structure, pipelines are subjected to service failures, due to corrosion, in oil and gas transporting media. The major focus of corrosion research in HSLA steels has been devoted in investigating their capability to resist the localized attack of the well-known forms of cracking such as Stress Corrosion Cracking (SCC), Sulfide Stress Cracking (SSC), and Hydrogen Induced Cracking (HIC)....etc [9,10,11,12,13].

Pitting, as the name suggests, is also a form of localized corrosive attack that produces pits. Pitting of pipeline steels caused by the chloride ions is one of the most destructive forms of corrosion as it could create perforation of equipment. It is well acknowledged in the literature that different types of localized attack; for example, SCC and pitting have several features in common. A quite number of studies observed that SCC and pitting were associated in adjacent or overlapping potential ranges [14] and SCC taking place in HSLA pipeline steels initiated from corrosion pits due to stress intensification in carbonate/bicarbonate environments containing chloride ions [15].

However, limited studies have been conducted to address the corrosion behavior, with a particular focus on pitting, on the newer generation of HSLA pipeline steels, API X-80 and API X-100 grades. This project primarily intends to provide an understanding and also a comparison on the electrochemical polarization behaviors of both aforementioned steels in free oxygenated bicarbonate/chloride media of various concentrations.

Specific objectives of the research are summarized as follows:

- Address the effect of bicarbonate ions with different concentrations on the corrosion polarization behaviors of steels
- Study the fundamental role of aggressive chloride ions on pitting corrosion susceptibility of steels and compare their resistance against pitting

- Investigate the influence of the microstructure and alloying elements of steels on the passive film properties and its stability in bicarbonate solutions with/without the presence of chloride ions
- Estimate and compare the corrosion rates for steels by means of the Tafel extrapolation method
- Examine the characteristic pitting features for steels in bicarbonate/chloride environments through the Scanning Electron Microscope (SEM) technique

CHAPTER TWO

2 Literature Review

2.1 Electrochemical Background

2.1.1 Corrosion Process Reactions

Basically, corrosion is the thermodynamic tendency for metal to react with its environment. In any corrosion process, the measure of reaction tendency can be expressed as an electrode potential. The electrode potential is measured as the difference between the equilibrium potential of a metal in contact with its ions at unit activity (concentration of metal ions is approximately 1N) and the potential of a reference electrode.

For convenience, the electrode potential of the following hydrogen reaction was arbitrarily selected as a reference and assumed to be equal to zero at all temperatures:

$$2H^{+}(aq) + 2e- \rightarrow H_2\,(gas) \qquad (2.1)$$

The electrode potentials of common elements with respect to the Standard Hydrogen Electrode (SHE) are tabulated in the standard electromotive force (emf) series in accordance with their tendencies to react. The more negative the value of the electrode potential, the greater the tendency for the metal to corrode.

In any corrosion cell, two chemical reactions are needed for the corrosion to take place. The first reaction is the oxidation of the metal (anode) by loss of electrons. For example, steel oxidizes according to the following the reaction:

$$Fe \rightarrow Fe^{2+} + 2e- \qquad (2.2)$$

The second reaction is the reduction reaction at the other electrode (cathode) and it occurs by absorbing these electrons. The reduction reaction of hydrogen represented by equation 2.1 is a good example in this case for steel, particularly in free oxygen environments.

2.1.2 Potential/pH Diagrams

Thermodynamic data regarding corrosion of metals in aqueous solutions is available in the form of E-pH diagrams called Pourbiax diagrams. In these diagrams, the regions of immunity, corrosion, or passivation of a metal at specific conditions of potential and pH are defined based on the knowledge of the most stable species of metal ions. Figure 2.1 illustrates the simplified potential/pH diagram under equilibrium conditions for the iron-water system at room temperature.

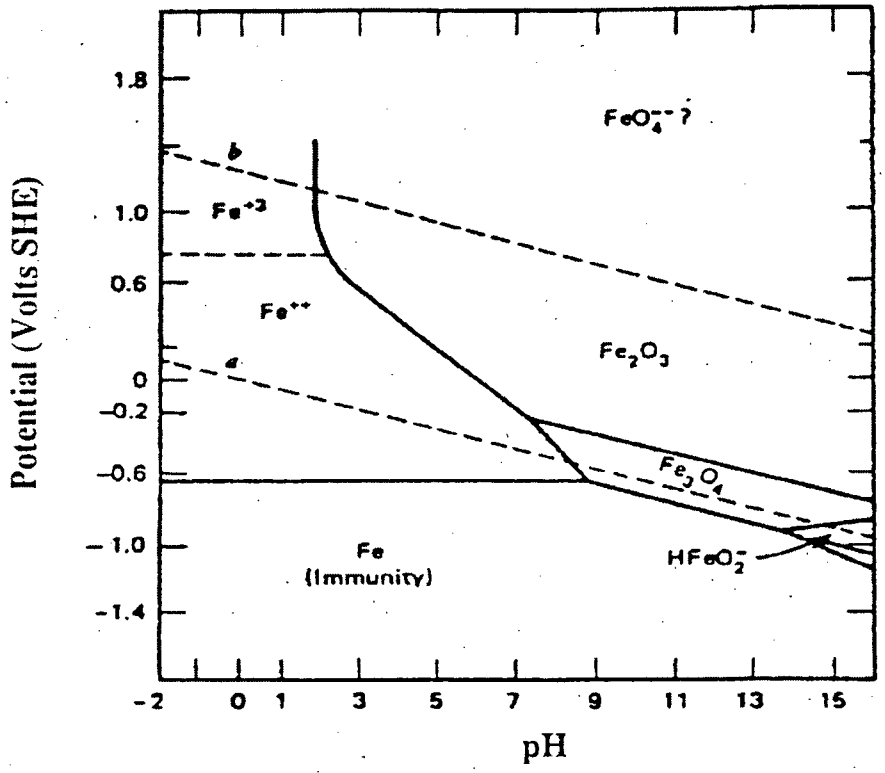

Figure 2.1 Simplified Pourbaix Diagram for the Fe-H_2O System at 25 °C [16]

The immunity region is the region where the metal is the most stable species and the concentration of soluble corrosion products (metal ions) would be less than 10^{-6} M. Corrosion occurs when the soluble corrosion products are the most stable. Passivation dominates when the insoluble corrosion product (oxides, hydroxides, etc.) are the most stable. The insoluble corrosion product forms a protective barrier between the metal and solution, preventing any further dissolution. The insoluble corrosion product may or may not be protective. With steel, for example, the scale is loosely adherent at pH 6 while strong and tenacious above pH 8, so passivation of steel at pH values below 8 is unlikely.

Passivation of steel is mainly related to the formation of a magnetite film (Fe_3O_4) which is a result of the following reaction [17]:

$$3Fe + 4H_2O \rightarrow Fe_3O_4 + 8H^+ + 8e^- \qquad (2.3)$$

The region between the two dashed lines, in figure 2.1, represents the theoretical limits of water stability. Hydrogen is evolved below line a, while oxygen is evolved above line b, respectively, according to:

$$2H_2O + 2e^- \rightarrow H_2 + 2OH^- \qquad (2.4)$$

$$2H_2O \rightarrow O_2 + 4H^+ + 4e^- \qquad (2.5)$$

A modification to the Pourbaix diagram may be needed since this data is essentially produced for pure iron and water, and does not provide a precise guide for complex environment/steel alloy systems. These modifications have taken other forms, for instance, potentiodynamic polarization curves.

2.1.3 Potentiodynamic Polarization Curves Technique

One electrochemical technique to define the region of immunity, corrosion, or passivation of an alloy in a complex environment is to generate potentiodynamic polarization curves, whereby the potential for the anodic or cathodic reactions (depending on the nature of the scan) is controlled, and the net change in the current is observed. The potentiostat measures the current

which must be applied to the system in order to achieve the desired increase in driving force, known as the applied current. As a result, at the open circuit potential (the potential at which the total anodic current is equal to the total cathodic current) the measured or applied current will be zero.

A series of potentiodynamic polarization scans are needed, each at a specific pH value. A sudden decrease in the measured current density corresponds to transitions from regions of corrosion to passivation. The diagrams for different pH values are then collected on one diagram showing the corrosion behavior of that particular alloy/environment system at a specific temperature.

Potentiodynamic polarization scans are also conventional electrochemical methods for pitting potential measurements. The pitting potential, the potential at which the passive film begins to break down locally, is one of the most important features characterizing the susceptibility of carbon steels to pitting corrosion.

The pitting potential is usually evaluated according to the shape of the anodic polarization curve. It is the potential value at which the current density starts to increase drastically in the passive range in solutions containing aggressive anions (e.g., Cl^-, etc.). This value is also called the breakdown potential. This value characterizes the resistance of the given metal or alloy to pitting in the given solution, and E_{pit} can therefore be considered a measure of the susceptibility of different metals and alloys to pitting in various aggressive environments.

The influence of different factors on pitting, for example, steel and solution composition, heat treatment, etc, can be evaluated by the determination of E_{pit}. The more positive E_{pit}, the more resistant is the material to pitting.

The following two subsections detail the features found on a typical anodic or cathodic potentiodynamic scan:

2.1.3.1 The Cathodic Polarization Scan

A schematic cathodic polarization scan is illustrated in figure 2.2. In a cathodic potentiodynamic scan, the potential is varied from point 1 in the negative direction to point 2. The open circuit potential (E_{op}) is located at point A. at this potential, the sum of the anodic and cathodic reaction rates on the electrode surface is zero. As a result, the measured current will be close to zero. This is due to the fact that the potentiostat only measures the current which it must apply to achieve the desired level of polarization.

Depending on the pH and dissolved oxygen concentration in the test solution, region B may represent the oxygen reduction reaction. Since this reaction is limited by how fast oxygen may diffuse in solution (mass transport controlled) there will be an upper limit on the rate of this reaction, known, as the limiting current density.

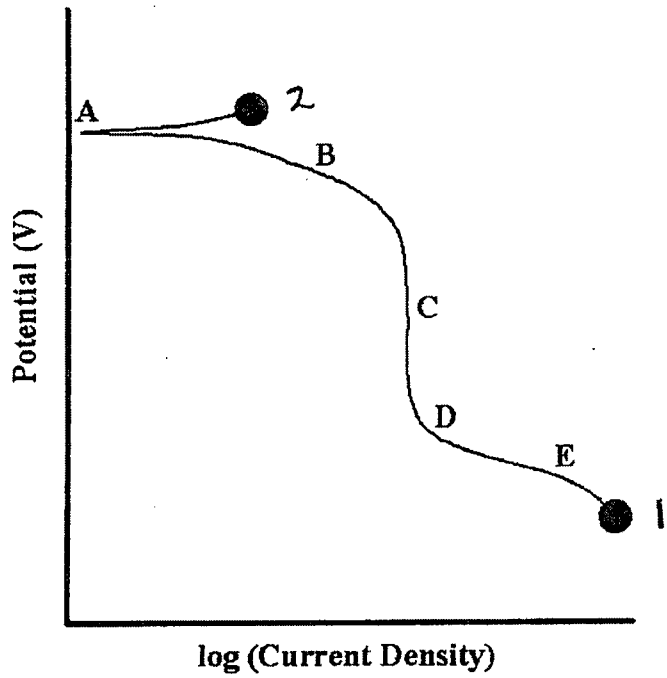

Figure 2.2 Typical Cathodic Polarization Curve [18]

Further decrease in the applied potential results in no change in the measured current (region C). Eventually, the applied potential sufficiently becomes negative for another cathodic reaction to become operative (i.e., there is sufficient thermodynamic driving force for an additional cathodic reaction to take place), such as illustrated at point D.

As the potential becomes increasingly large, this reaction may become dominant, as illustrated in region E. This additional reaction is typically the reduction of the species in the environment (such as the hydrogen evolution reaction, also known as the water reduction reaction). An increase in current may also be observed if sufficient potential exists to reduce the oxide present on the electrode surface.

2.1.3.2 The Anodic Polarization Scan

A schematic anodic polarization curve is illustrated in figure 2.3. As can be seen in the figure, the scan starts from point 1 and progresses in the positive potential direction until termination at point 2. There are a number of notable features on the curve. As with the cathodic scan, E_{op} represents the potential at A, at which the sum of the anodic and cathodic reaction rates occurring on the electrode surface is zero.

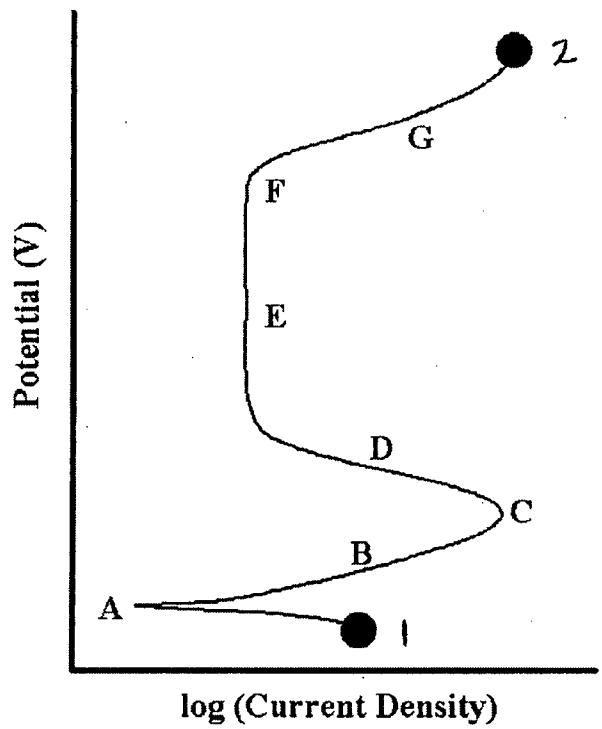

Figure 2.3 Typical Anodic Polarization Curve [18]

As the potential increases, the curve reaches region B, which is the active dissolution region. In this region, metal oxidation (Fe in HSLA case) is the dominant reaction taking place. Point C is known as the passivation potential, and as the applied potential increases above this value the

current density is seen to decrease with increasing potential (region D) until a low, passive current density is achieved (passive region –region E).

Once the potential reached a sufficiently positive value (point F, sometimes termed the breakdown potential or the pitting potential, E_{pit}) the applied current rapidly increases (region G). This increase may be due to a number of phenomena, depending on the alloy/environment combination. For some systems (e.g., HSLA steels in salt water) this sudden increase in current may be due to pitting (localized breakdown of passivity), while for others it may also be combined with trans-passive dissolution and then oxygen evolution depending on the nature of a particular system.

2.1.3.3 Corrosion Rate Calculations

One of the pieces of information often extracted from potentiodynamic polarization curves is the corrosion rate. For reactions which are essentially activation controlled (i.e., charge transfer controlled reactions, or mass transfer controlled reactions occurring at a rate much less than the limiting rate), the current density can be expressed as a function of the overpotential, η, where $\mu = E_{applied} - E_{op}$ as follows [19];

$$\eta = \beta \log (i/io) \qquad (2.6)$$

This equation is known as the Tafel equation, where:

β: The Tafel slope

i: The applied current density

i_o: The exchange current density (the reaction rate at the reversible potential for that particular reaction)

Thus, the Tafel slope for the anodic and cathodic reactions occurring at open circuit may be obtained from the linear regions of the polarization curve, as illustrated in figure 2.4. Once these slopes have been established, it is possible to extrapolate back from both the anodic and cathodic regions to the point where the anodic and cathodic currents are equal. The current density at that point is the corrosion current density (i_{corr}) and the potential at which it occurs is the corrosion potential (E_{corr}).

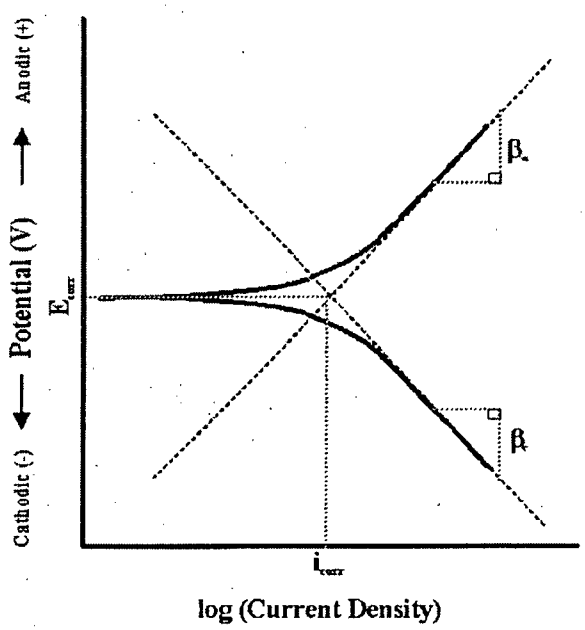

Figure 2.4 Tafel Slope Calculations Graph

The corrosion current density may then be combined with Faraday's law [19]:

$$\textit{Corrosion rate (mpy)} = \frac{0.129 \times i_{corr}(\mu A/cm^2) \times EW}{\textit{Density } (g/cm^3)} \qquad (2.7)$$

This equation will be used in this paper to calculate the corrosion rates of API X-80 and API X-100 steels in which:

EW: the equivalent weight, indicating the mass of metal in grams, which is oxidized. For carbon steels, the EW is approximately 28 grams.

Density: 7.84 g/cm^3 for carbon steels.

2.1.4 Localized Corrosion Mechanisms

The pitting corrosion of metals has been commonly considered as being developed in two stages: initiation and propagation. Although there is general agreement concerning the mechanisms of propagation stage which involves the continued stable growth of the corroding area, doubts still remain on the processes leading to the initiation of pits on the surface of the passive film [20].

A number of models have been proposed to describe the initiation of localized corrosion of passive metals based either on the breakdown processes of the passive film itself or on

structural defects or heterogeneities of the underlying metal or alloy such as dislocations, grain boundaries, second-phase precipitates, or nonmetallic inclusions. Certainly a strict differentiation of the two approaches is not always possible, since film breakdown and structural parameters of the underlying metal may be correlated [21].

Theoretical models that describe the initiation process leading to passive film breakdown may be grouped into three classes: (1) adsorption-induced mechanisms, where the adsorption of aggressive ions like Cl^- is of major importance, (2) ion migration and penetration models, and (3) mechanical film breakdown theories, as shown in figure 2.5 [22].

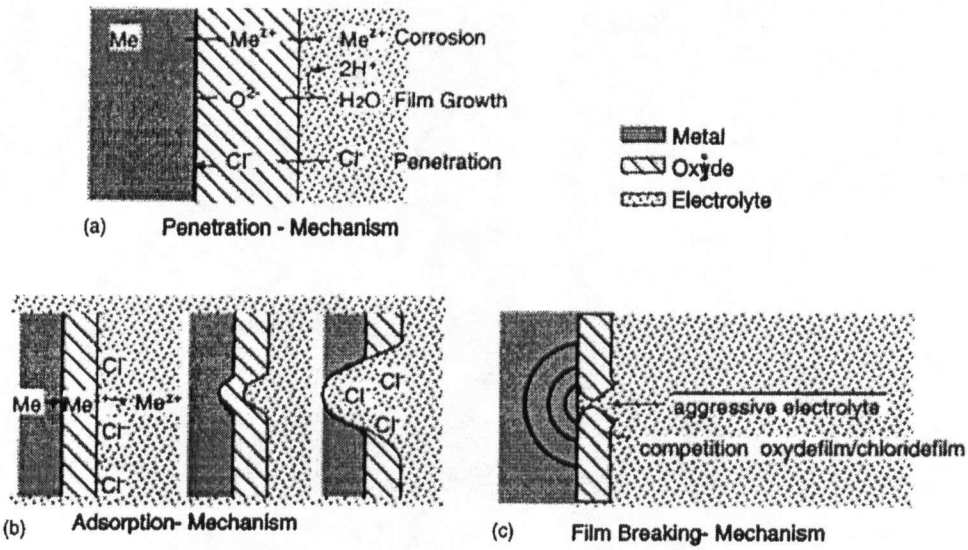

Figure 2.5 Models for Pit Initiation Leading to Passive Film Breakdown [22]

Of various theoretical models describing pitting initiation such as the aforementioned ones, there is a common requirement for the initiation of the pits: adsorption of aggressive ions like the chloride ions. However, the role of chloride ions in pitting process, particularly during the initiation stage, is controversial. Newman [23] thought that Cl^- increased the conductivity of

electrolyte and then the dissolution rate to support activation of the pit sites. Galvele's results [24] showed that maintaining sufficient transport of Cl^- from the bulk electrolyte to the pits was the necessary condition to sustain the propagation of the metastable pit.

Hoar and Jacob [25] proposed a theory of the chemical dissolution and thought that the breakdown of the passive film is caused by the formation of soluble complex ions between the chloride ions and metals and oxides. Others thought that the main role of Cl^- lied in increasing the initiation process itself by increasing the number of susceptible sites [26] or decreasing the pitting potential [27].

Work performed by Simard et al. [28] showed that the resistance of passivated mild steel to localized corrosion induced by Cl^- is closely linked to the pre-anodization potential. Below 0.3 V, the breakdown of the film begins by a thinning of the passive film due to a catalytic dissolution and followed by Cl^- reaching the metal surface. At this time, a severe localized attack occurs. Over 0.3 V of the pre-anodization potential, the film become more stable and loses its sensitivity to pitting attack.

2.1.5 Pits Nucleation Sites

The surface of every piece of metal or alloy has some physical or chemical inhomogeneities that can be more susceptible to attack in aggressive environments compared with the remaining surface; it is generally acknowledged that this increased susceptibility is related to local imperfections of the passive film on the surface being considered [27, 29].

Alloying elements that improve passivity of steels such as Cr and Mo are known to increase the steel resistance to pitting. On the other hand, some nonmetallic inclusions, e.g., sulfides and complex sulfide-oxide inclusions and second phase precipitates, are able to nucleate pits in a variety of iron based alloys [29]. There is a generally accepted belief that passive films, which exhibit the more effective protective properties, form on chemically and physically homogeneous metal surfaces [30].

Commercial materials often contain large amounts of impurities and nonmetallic inclusions. For example, the number of inclusions emerging on the surface of ordinary low alloy or stainless steels of current industrial production was estimated at $1000/cm^2$ [27]. Therefore, it has to be dealt with inhomogeneous metal surfaces. When the surface layer of metal contains some chemical inhomogeneities or physical defects, localized attack is likely to be initiated at these weak spots. It can be anticipated that inhomogeneities in the chemical composition of the surface will affect the protective properties of passive films more strongly than physical defects.

According to Smialowska [27], as far as chemical inhomogeneities are concerned, the following features are thought to induce formation of weak spots in the passive film.

1) Boundaries between the metal matrix and nonmetallic inclusions where differences in coefficients of thermal expansion exist.

2) Boundaries between the metal matrix and second phase precipitates often have the ability to deplete from the alloy some components responsible for the passive state such as Cr impoverishment of Cr-Ni steels as a result of chromium carbide formation.
3) Inclusions having greater chemical reactivity compared with that of the metal or alloy itself.

Because of the extreme technical importance of iron base alloys and their susceptibility to pitting, particularly numerous and extensive investigation have been undertaken to identify the most probable sites of pit nucleation in various steels particularly on the dominant role of sulfide inclusions in pitting [31,32,33]. From the chemical point of view, many explanations on the role of the MnS inclusions in pitting corrosion of steels are based on a detrimental influence of specific dissolution products of the sulfides. A detailed investigation demonstrated that the corrosive attack of the MnS inclusions is accompanied by a release of sulfur was found to depend on the pH of the solution. The chemical and/or the electrochemical reactivity of inclusions of different compositions, or synthetic inclusions, have been addressed [34].

Sulfur is present as an impurity in all commercial steels and in pure metals such as in the case of iron. Because of its low solubility in iron and iron base alloys, sulfur precipitates in the form of sulfide particles or complex oxide-sulfide inclusions. Ordinary carbon steels contain MnS, FeS, (Mn,Fe)S, and CaS [35].

Thermodynamic calculations support the idea that manganese sulfide can act as a pit initiation site. The potential-pH diagram calculated for the Mn-H_2O- Cl^- system is shown in figure 2.6. The

diagram is applicable only to relatively concentrated solutions (e.g., 0.1M Mn species); it may be somewhat different for more dilute solutions. However, it is useful in defining the dissolution behavior of MnS. For example, it shows that MnS can exist between pH 4.8 and 13.8. At pH values less than 4.8, MnS dissolves to form H_2S and various manganese ions. However, even at the pH ranges 4.8-13.8, the highest potential at which MnS can exist is about -100 mV (at pH 5). At more noble potentials, MnS dissolves to yield sulfur [36]. An important conclusion that emerges from the potential-pH diagram shown in figure 2.6 is that manganese sulfide inclusions are active anodic sites at a steel surface in the presence of aqueous chloride solutions.

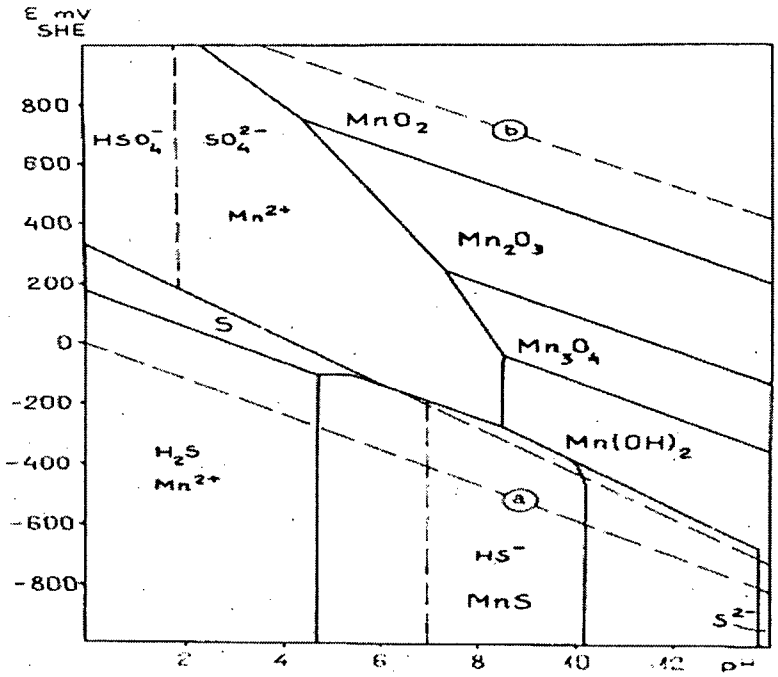

Figure 2.6 Potential-pH Diagram for Mn-H_2O-Cl^- System calculated on the basis of 0.1 M for sulfate, chloride and manganese ions [36]

The question of why carbon steels initially exhibit pitting when exposed to neutral NaCl solutions may be raised. This phenomenon can be caused by different factors. As is known, these

steels are usually coated with a very thin (approximately 10A) air formed oxide film. The results of the electrochemical studies have shown that this film is non-protective; when exposed to aqueous electrolytes, the underlying metal assumes a potential corresponding to active dissolution. On the other hand, some differences may occur in the dissolution rate at certain areas covered with a more or less tight oxide film. It is possible that localized attack can also be caused by selective dissolution of sulfides situated in the surface layer of the metal [27].

Carbon steels usually contain mixed iron-manganese sulfides with various concentrations of iron. The properties of iron sulfide differ from those of manganese sulfide. Iron sulfide exhibits a lower dissolution rate in aqueous solutions and a higher electrical conductivity. The conductivity of mixed Mn-Fe sulfides depends on the FeS:MnS ratio, which is dependent on the Fe:Mn ratio in the steel being considered.

In aqueous environments, it has been established that Sulfides rich in Mn are easily attacked by corrosive media, while sulfides rich in Fe are not. Around Mn-rich sulfide inclusions, crevices often form and both the inclusion and the matrix are attacked, while in the case of Fe-rich sulfides, the adjacent metal is attacked but the inclusion is not. However, Mn-rich sulfide inclusions may occur even in Mn-poor steels and this leads to severe pitting. Because MnS can be detected in all pits regardless of its concentration in the steel, it can be concluded that pits form predominantly at Mn-rich sulfide inclusions [27, 38].

Regarding compositional modification of the sulfide, the main emphasis has been either on reducing the manganese content of the bulk steel or adding rare earth metals (mainly Cerium). It

has been found that the chromium content of sulfide inclusions increases when the manganese content is decreased. The chromium-containing sulfide appears to be a less effective nucleation site for pitting than manganese sulfide [28].

2.1.6 Pitting and Other Types of Localized Corrosion

It is well known that different types of localized attack, crevice corrosion, pitting, stress corrosion cracking (SCC) and corrosion fatigue have several features in common. SCC has been often observed to initiate from corrosion pits or crevices in industrial practice. The nucleation of stress corrosion cracks from corrosion pits has been observed for many metals and alloys such as HSLA steels in the literature.

Localized corrosion processes for iron and carbon steels in carbonate/bicarbonate media have been extensively studied in relation with intergranular SCC phenomena in gas or oil transportation pipelines. SCC occurs in a narrow potential range (situated at the active to passive transition) as a result of a competition between film growth and metal dissolution induced by mechanical breakdown of the passive layer [39].

It is generally acknowledged that the surface layers are very much involved in this sort of damage. A number of studies are available about the properties of the corrosion products or iron and carbon steels in an HCO_3^-/CO_3^{2-} environments. These studies indicated the presence of primarily $Fe(OH)_2$, $FeCO_3$ (siderite) and γ-Fe_2O_3 (magnemite) and sometimes Fe_3O_4 (magnetite) as solid species, together with complexes such as $Fe(OH)^+$, $Fe(H_2O)_6^{2+}$, $FeHCO_3^+$, $Fe(CO3)_2^{2-}$,

$Fe(HCO_3)_{2(aq)}$ with as dissolved species, each of them being involved with one of the activation peaks recorded in the anodic range on the polarization curves [40,41,42,43].

Chen et al. [44] studied the mechanisms of SCC initiation in X-65 pipeline steel exposed to environment containing HCO_3^-/CO_3^{2-} and Cl^- ions under a mechanical loading typical of a pipeline operating in the field. He found that micro-cracks were initiated mostly from the corrosion pits at metallurgical discontinuities such as grain boundaries, pearlitic colonies and banded phases in the steel.

In addition, Yu et al. [10] addressed the effect of the electrochemical potential, pH value, and the hydrogen ingress on the trans-granular stress corrosion cracking (TGSCC) of API X-52 and API X-80 pipeline steels using the slow strain rate testing in solutions consisting of HCO_3^-/CO_3^{2-} and Cl^- ions. He found through the SEM observations that extensive pitting occurred on the surface of the specimens and those corrosion pits should have been involved in initiating the TGSCC cracks.

Park et al. [45] investigated the effect of oxide film passivity on low-pH SCC of API X-65 pipeline steel in HCO_3^- solution using the potentiodynamic polarization scans. From the observations of the SEM after the slow strain rate test (SSRT), he found that stress corrosion failure mode in low-pH HCO_3^- solution is TGSCC and it was developed by a pit-to-stress corrosion crack transition mechanism.

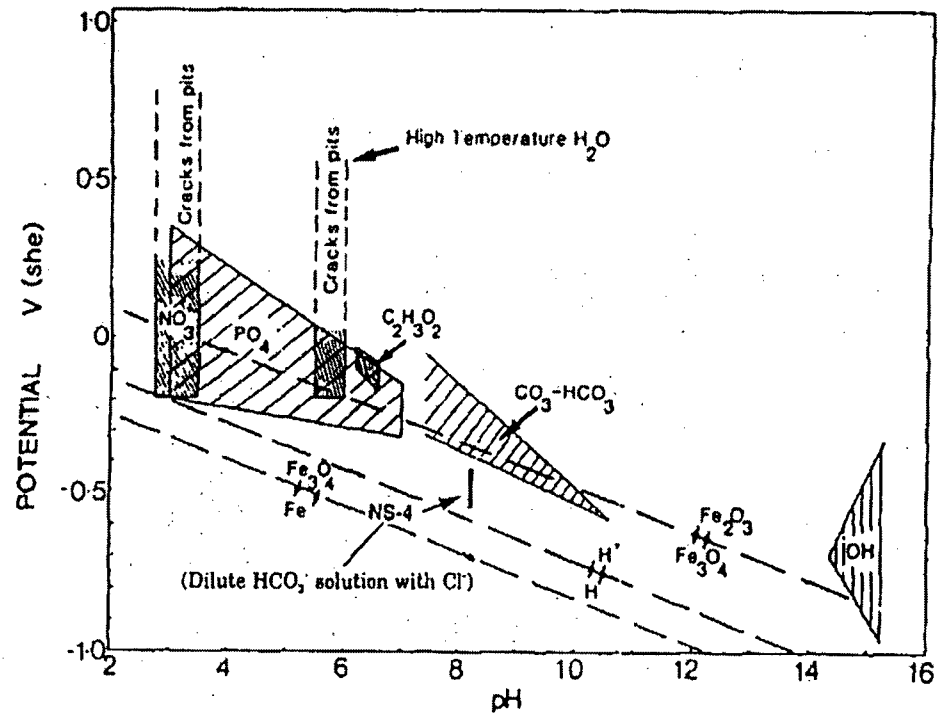

Figure 2.7 Potential and pH Ranges for the SCC of Steels in Various Environments including Bicarbonate Ions associated with Chloride Ions [46]

Figure 2.7 shows the SCC region for carbon steel in (0.5 to 1M) CO_3^{2-}/HCO_3^- solution(published by Parkins [46,47]), where the passive film exists and the SCC is due to film rupture and dissolution [46,47].

2.2 Corrosion of Low Alloy Steels in Carbonate/Bicarbonate Media

2.2.1 Main Reaction Processes

Localized corrosion in carbonate/bicarbonate (CO_3^{2-}/HCO_3^-) environments is a great concern in the oil industry. CO_3^{2-}/HCO_3^- media results from the practice of pumping CO_2 saturated water into wells to enhance oil recovery and reduce the viscosity of the pumped fluid. The presence of CO_2 leads to the formation of a weak carbonic acid (H_2CO_3) which drives CO_3^{2-}/HCO_3^- corrosion reactions. This initiating step is represented by the reaction shown in equation 2.8:

$$CO_2 + H_2O \leftrightarrow H_2CO_3 \tag{2.8}$$

The subsequent corrosion process is controlled by three cathodic reactions and one anodic reaction [48]. The cathodic reactions (given in equation 2.9) include (a) the reduction of carbonic acid into bicarbonate ions, (b) the reduction of bicarbonate ions into carbonate ions, and (c) the reduction of hydrogen ions to hydrogen gas.

$$2H_2CO_3 + 2e^- \rightarrow H_2 + 2HCO_3^- \tag{2.9a}$$

$$2HCO_3^- + 2e^- \rightarrow H_2 + 2CO_3^{2-} \tag{2.9b}$$

$$2H^+ + 2e^- \rightarrow H_2 \tag{2.9c}$$

The anodic reaction significant in localized corrosion in carbonate/bicarbonate media is the oxidation of iron to the ferrous (Fe^{2+}) ion given in equation 2.2. Since localized corrosion of low alloy steels in oil and gas wells containing carbonate/bicarbonate ions occurs in anaerobic conditions, oxidation to the ferric (Fe^{3+}) ion is not included here.

$$Fe \rightarrow Fe^{2+} + 2e^{-} \tag{2.2}$$

These corrosion reactions provide a chemical environment which promotes the formation of iron carbonate ($FeCO_3$). $FeCO_3$ can form a long a couple of reaction paths [49]. First it may form when ferrous ions react directly with carbonate ions as shown in equation 2.10. However, it can also form by the two step process shown in equations (2.11a, 2.11b). When ferrous ions react with bicarbonate ions, iron bicarbonate forms which subsequently dissociates into iron carbonate along with carbon dioxide and water.

$$Fe^{2+} + 2CO_3^{2-} \rightarrow FeCO_3 \tag{2.10}$$

$$Fe^{2+} + 2HCO_3^{-} \rightarrow Fe(HCO3)_2 \tag{2.11a}$$

$$Fe(HCO3)_2 \rightarrow FeCO_3 + CO_2 + H_2O \tag{2.11b}$$

The significance of $FeCO_3$ formation is that it drops out of solution as a precipitate due to its limited solubility (Ksp = 10.54 at 25 °C) [50]. This precipitate has the potential to form passive films on the surface of HSLA pipeline steels which may reduce their corrosion.

2.2.2 Effect of Alloying Elements and Microstructure

The final microstructure of HSLA line pipe steels is determined by its chemical composition and the thermo-mechanical treatments used during the production processes. Although the design criteria are mainly focused on the properties such as mechanical resistance, toughness, and weldability, the corrosion resistance is also affected.

The microstructure is considered to have a significant effect on how firmly the corrosion scale sticks to the surface. The adherence of the corrosion product film, and hence its protectiveness, has often been related to the presence of iron carbide and its morphology (laminar, globular, etc.). The idea is that the carbide phase can strengthen the film and can anchor it to the steel substrate, and then the size and distribution of these carbides become very important [51]. However, the accumulation of carbides in the corrosion product has been seen as the cause of increasing corrosion rate over time of exposure for ferritic/pearlitic (F/P) steels [52, 53].

Crolet et al. [53] discussed the role of conductive corrosion product in the protectiveness of surface layers. They established that corrosion layers containing the same components could be extremely protective, very little so, or even corrosive depending on the location of these components. According to theses authors, a thin layer of hollow Fe_3C in contact with the steel is sufficient to cause the onset of internal acidification. Provided that a high enough iron concentration is present in the test solution when the freshly polished specimens are immersed, $FeCO_3$ precipitates on the metal surface and the layer then becomes protective. If the iron content

increases only after an initial phase of the corrosion leading to the formation of an empty Fe_3C layer, then internal acidification prevents further precipitation of $FeCO_3$ on the metal, even though the outer part of the layer becomes obstructed. In this last case the resulting layer is not protective.

At present there is no common agreement about the mechanism and the way in which microstructure and heat treatment affect the growth and stability of iron carbonate film. It has been reported that plain normalized carbon steel with a ferritic/pearlitic microstructure is far superior to the quenched and tempered alloy steel with a martensitic microstructure and vice versa [51].

Stegman et al. [54] addressed the role of temperature, the chloride additives, and the metallurgy on flow induced localized corrosion. They used steel tubing with six dissimilar compositions and they found a better corrosion resistance for the quenched and tempered samples compared to the ferrite/pearlite ones. They proposed that the needle-like carbide structure provides a better fastening surface for the $FeCO_3$ than large ferrite areas inter-mixed with a few pearlite grains. On the other hand, when they compared two N80 grade steels having the same composition but different microstructure (ferrite/pearlite vs. martensite/bainite) they did not find marked variations with respect to the corrosion rates.

Ueda and Takabe [55] also studied the effect of the environmental factors and microstructure on the morphology of the corrosion products in bicarbonate/carbonate systems with a 5% NaCl. They used two different steels: J55 and N80. The J55 specimens had a ferrite/pearlite

microstructure while the N80 ones had a tempered martensite. Corrosion rates were performed by means of weight loss measurements. The authors found that N80 steel showed a lower corrosion rates than J55 steel, but suffered pitting corrosion. $FeCO_3$ was identified by X-ray analysis in the corrosion products for both steels. The good pitting corrosion resistance of the J55 steel was due to the presence of lamellar cementite embedded in the film. In the N80 steel the cementite is homogenously dispersed in the martensitic microstructure and due to the lack of anchoring, the corrosion products peel off partially.

Cui et al. [56] investigated the pitting corrosion behavior of carbon steels with different banded microstructures in chloride solutions using the in situ scanning reference electrode technique (SRET). The specimen surfaces were inspected with an optical microscope after SRET measurements and the variation of potential over the test surface was compared with the corrosion morphology. Pitting susceptibility was found to vary with microstructure of the steel. The surface morphology showed that pits were predominately initiated on the ferrite bands for specimens with martensite-ferrite microstructure, but preferentially on martensite for specimens with martensite/pearlite structure.

Niece and Uede [57] pointed out the significance of steel microstructure and chromium alloying content from failure analysis of corroded well tubing steel grade L-80 employed for sea water injection service. They found marked differences in the corrosion resistance performance for steels specified as API 5CT grade L-80 received from different steel manufactures. They indicated that the combination of a quenched and tempered martensitic microstructure with chromium content within 0.5-1.0 wt.% offered a better corrosion resistance than either this

microstructural condition or the combination of a quenched and tempered bainitic/martensitic microstructure with little or no chromium content (< 0.1 %). They stated that the role of the microstructure in improving the steel corrosion resistance is not completely obvious.

Lopez at al. [58] studied the characteristics of corrosion layers (morphology, thickness and composition) formed on a carbon steel with two different heat treatments (annealing and tempering). The characterization was made by means SEM method, Electron Dispersive X-ray (EDX) and X-ray Photoelectron Spectroscopy (XPS). The test solution was 5 wt.% of NaCl, saturated with deoxygenated CO_2 at pH 6 and 40 °C. From the results, it was concluded that the microstructure of the steel influences the properties of the corrosion layers, such as morphology and proportion of the various chemical compounds present.

Nice et al. [59] studied the effect of both chromium addition (up to 10%) and the microstructure on general and localized corrosion in production well environments. They performed autoclave tests varying the temperature between 60 and 100 °C, the gas composition (a mixture of CO_2 and H_2S) and the flow velocity (1 and 2.5 m/s). They employed a wide variety of steels with different chemical compositions and microstructures. The corrosion rate observed for chromium steels was smaller than that of carbon steels. However, chromium bearing steel with a ferrite/pearlite microstructure presented a lower corrosion resistance than with a martensitic one. The authors consider that the inhomogeneous ferrite/pearlite microstructure interferes in the formation of a homogeneous chromium rich film on the steel surface.

Furthermore, they [59] analyzed the corrosion deposits by means of X-ray and EDX techniques. $FeCO_3$ was identified in almost all the corrosion deposits and an enrichment of chromium content was observed by EDX for the chromium bearing steels. They found as well that the minimum chromium content required to reduce corrosion rate was a function of the test temperature. At 60 °C, a beneficial effect was obtained when the chromium content was above 1%, at 80 °C; a reduction in the corrosion rate was observed for chromium additions above 0.5% whilst 1% addition was needed to decrease the corrosion rate at 100 °C.

Kermani et al [60] showed a number of low carbon steels containing different alloying elements presented improved corrosion resistance in bicarbonate/carbonate media by a factor of 3-10 while maintaining their cost to no greater than 1.5 times that of conventional grades of carbon steels. They studied the effect of Cr additions up to 3%, micro-alloying elements (V, Ti, Mo and Nb) were used to maximize the effect of a given addition of Cr by ensuring that it remained in solid solution in the matrix rather than forming carbides.

Besides, they [60] added Si (0.3- 1%) to help bainite formation under normal conditions. Their electrochemical measurements indicated that Cr content is detrimental to the anodic reaction at the lowest concentration and thus can lead to inconsistency in the corrosion performance of low Cr containing steels. At 3% Cr or more, protective films form at conditions in which $FeCO_3$ films are hardly stable and they can grow at a pH as low as 5. Using 3% Cr, 0.6 Si and Mo, V, and Cu additions in a low carbon steel they obtained an improvement in corrosion resistance of more than five times compared to standard API X-70 grade steel.

2.2.3 Effect of Environmental Factors

2.2.3.1 Oxygen Content

$FeCO_3$ is unstable in the presence of oxygen, thus passive $FeCO_3$ films normally form under anaerobic conditions. In field applications, oxygen may enter production equipment due to water or inhibitors injection. The oxygen concentration should be kept under 40 parts per billion (ppb) in order to suppress the oxidation of ferrous ions (Fe^{2+}) into ferric ions (Fe^{3+}). In addition to the modification of the film stability, a higher oxygen concentration contributes to the increase rate of the cathodic reaction (oxygen reduction) [61].

2.2.3.2 Iron Content

The content of ferrous ion in solution determines if it is possible to form $FeCO_3$ or not, as it is necessary to exceed the solubility limit in order to precipitate iron carbonate. The $FeCO_3$ growth rate depends on the temperature and on the level of super-saturation [62].

2.2.3.3 pH Value

Uniform corrosion rate in HCO_3^-/CO_3^{2-} decreases as the system pH increases. This is related to the decrease in the solubility of $FeCO_3$ which in turn makes the formation of a protective film more feasible as can be seen by equations 2.9a, 2.9b and 2.9b [63].

2.2.3.4 CO_2 Content

The uniform corrosion rate increases with higher CO_2 partial pressure because the solution pH decreases and the rate of reduction of carbonic acid increases as can be seen by equations 2.9a, 2.9b and 2.9b [64].

2.2.3.5 Flow

Usually the corrosion rate increases with flow velocity due to one or more of the following causes: preventing formation of passive $FeCO_3$; removing existing films or retarding the growth of such films by enhancing mass transfer of reactants near the surface [51, 63].

2.3 High Strength Low Alloy Steels Developments

2.3.1 Overview

In the last 30 years, large demands have been placed on the pipe manufacturer with respect to the development and the processing of materials to pipeline. Generally, longitudinally welded large diameter pipeline is used for the transportation of oil and gas, because it offers the highest safety in pipeline operation and represents the most economic solution. From the point of view of pipeline economy, the pipe must favorably respond to laying in the field and permit high operating pressures for the pipelines. These requirements imply that the pipeline steel has to possess high strength and toughness and that the pipe shall have optimized geometry.

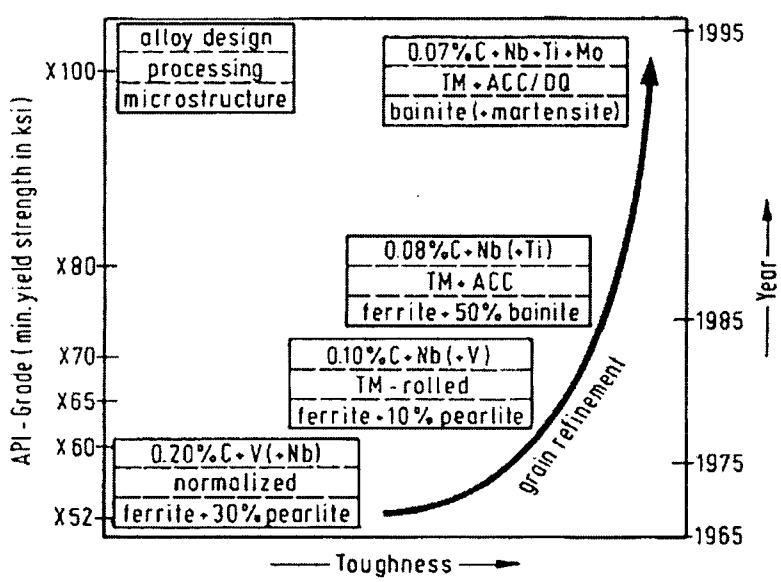

Figure 2.8 Development of High Strength Low Alloy Steels [65]

The development of high strength steels is illustrated in figure 2.8 [65]. In the seventies, the hot rolling and normalizing was replaced by thermo-mechanical rolling. The latter process enables materials up to X-70 to be produced from steels that are micro-alloyed with niobium and vanadium and have reduced carbon content. An improved processing method, consisting of thermo-mechanical rolling plus subsequent accelerated cooling, emerged in eighties. By this method, it has become possible to produce higher strength materials like X-80, having a further reduced carbon content and thereby excellent field weldability. Additions of molybdenum, copper and nickel enable the strength level to be raised to that of grade X-100, when the steel is processed by thermo-mechanical rolling plus modified accelerated cooling.

2.3.2 Effect of Microstructure

Microstructural features such as dislocation, grain boundaries and precipitation, govern the mechanical properties of steels. In low alloy steels, they develop in the course of transformation of the austenite during cooling, and the development depends on the cooling rate and cooling stop temperature.

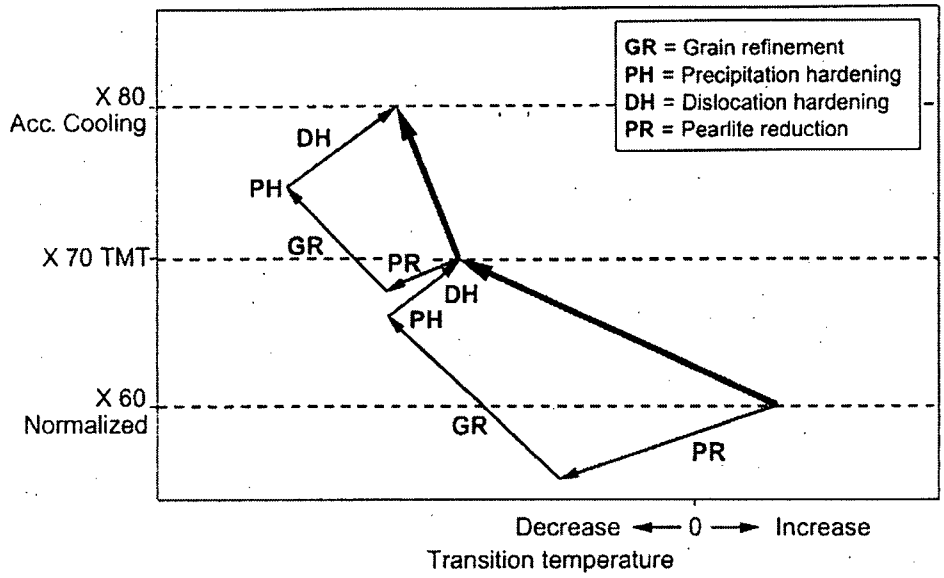

Figure 2.9 Effect of Microstructure on Strength and Toughness [66]

Figure 2.9 shows, how the combination of the various types of microstructures contribute to increase the mechanical strength and toughness of steels starting from normalized X-60 grade, which was mainly used in early seventies [66]. The steel typically contains about 0.2% carbon, 1.55% manganese, 0.12% vanadium, 0.03% niobium, and 0.02% nitrogen.

The thermo-mechanically processed X-70 steel mentioned in the figure was micro-alloyed and contains only 0.12% carbon. Thermo-mechanical rolling results in a significant reduction of the ferrite grain size. Grain refinement is the only method by which both strength and toughness can simultaneously be improved. The loss of strength resulting from reduced pearlite contents can be offset by precipitation hardening and dislocation hardening. Reduction of pearlite content, grain refining, dislocation hardening and precipitation hardening contributed individually and in

combination to the development of X-70 steel with improved weldability and favorable ductile-brittle transition temperatures. Further increase in strength and toughness, which led to the development of X-80 steel, can only be attained by changing the microstructure of the steel matrix from ferrite/pearlite to ferrite/bainite. In comparison with the thermo-mechanically rolled X-70 steel, the X-80 steel has further reduced carbon content, reduced grain size and increased dislocation density [66].

2.3.3 Effect of Alloying Elements

The micro-alloying of steels with the addition of small amounts of strong carbo-nitride forming elements in conjunction with controlled rolling practices has achieved a great improvement in their mechanical properties. The alloying elements improve the mechanical properties through many factors, the most important of which [67] are:

- Refinement of the ferrite grain size by the formation of a fine sub-grain structure
- Strain induced precipitation of the carbides and nitrides of the strong carbide and nitride forming elements
- Precipitation strengthening of the ferrite

Titanium, niobium, vanadium are the most commonly used alloying elements to precipitate as carbo-nitrides and induce the grain refinement in steels. Apart from these,

other elements such molybdenum, copper, nickel, aluminum are added to these steels [68].

2.3.4 Thermo-Mechanical Rolling and Accelerated Cooling

In order to achieve a homogeneous fine grained microstructure and hence improved strength, toughness and cracking resistance, compared to steels produced by conventional thermo-mechanical rolling, the accelerated cooling process is adopted in the plate mill.

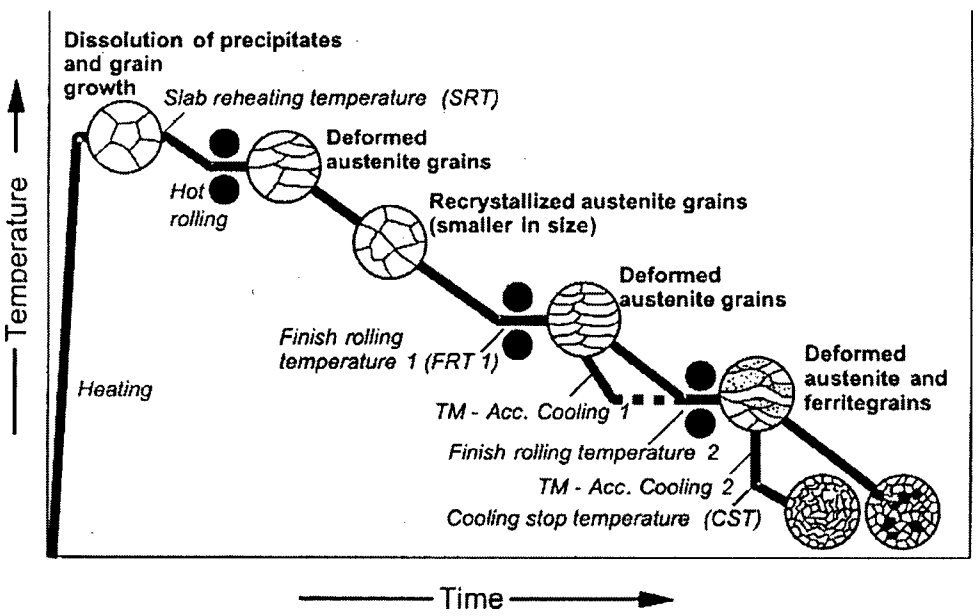

Figure 2.10 Schematic Illustration of Thermo-Mechanical Rolling with and without Accelerated Cooling during the 2nd and 3rd Rolling Stage [69]

The metallurgical processes occurring during thermo-mechanical rolling in conjunction with accelerated cooling can be understood from the schematic diagram

presented in figure 2.10 [69] in which the most significant rolling parameters to be controlled are shown.

The cooling system used here can be put into operation twice during rolling. Cooling operation 1 enhances the grain refinement of ferrite, whereas cooling operation 2 prevents the formation of pearlite during cooling, thereby improving the homogeneity of the final microstructure. Important variables of the cooling operations are cooling rate and cooling stop temperature. This special cooling system permits cooling to be carried after the second and third stages of rolling since it is firstly, quite compact, and secondly, installed close to the rolling stand.

The fundamental rolling parameters of the thermo-mechanical process are:

- The slab reheating temperature (SRT) for dissolution of the precipitated carbo-nitrides
- The roughing phase for producing a fine, polygonal austenite grain by means of re-crystallization
- The final rolling temperature (FRT), which must be maintained within the range of the non re-crystallizing austenite
- The degree of the final deformation (FD) at this temperature

If accelerated cooling is employed, the following parameters shall be considered:

- The cooling rate
- The cooling stop temperature (CST)

2.3.5 Pipeline Steels Developments

Accelerated cooling after rolling introduced the possibility of cost-effective production of new generation of pipeline steels with higher strength. This section will mainly focus on API X-80 and API X-100 steels developments.

2.3.5.1 API X-80 Steels

The typical layout of an accelerated cooling allows a cooling rate of 15 to 20 °C/sec and applies a cooling stop temperature of around 550 °C, followed by air cooling. With the typical chemical composition of X-70 steel of around 0.1% carbon and 1.5% manganese, the resulting steel is X-80 with a final microstructure of ferrite with a certain amount of bainite. In order to increase the strength without impairing the toughness, one aims for a higher volume fraction of bainite, and this usually obtained by increasing the hardenability of steel, i.e. by adding more alloying elements which retard the transformation, such as manganese, molybdenum or nickel.

Moreover, efforts have been undertaken to maximize the effect of niobium: when the nitrogen of the steel is fixed by an element exhibiting a higher affinity than niobium, e.g. by titanium, then more than the conventional niobium content will be dissolved during the slab reheating, which allows for more intensive austenite

processing and opens up the possibility of increased hardenability and more precipitation hardening by niobium carbides [70].

The X-80 alloy design is based on a higher manganese level than that known for the X-70 steel allowing for transformation into a more bainitic microstructure via accelerated cooling after thermo-mechanical rolling. In order to assure the high tensile strength, the carbon content had to be kept to a fairly high level. Since the nitrogen is fixed by titanium, the more effective use of niobium in this steel results in a condition where no other micro-alloy additions are required.

2.3.5.2 API X-100 Steels

No technological breakthroughs, such as rolling and accelerated cooling with increased strength and toughness respectively, but only improvements in the existing technology were involved in the production of X-100 grade. As a result, the production window is quite narrow. Heat treatment of plate or pipe is clearly not advisable.

As can be seen in figure 2.11, three different approaches are commonly possible in terms of the selection of chemical composition and cooling conditions [71].

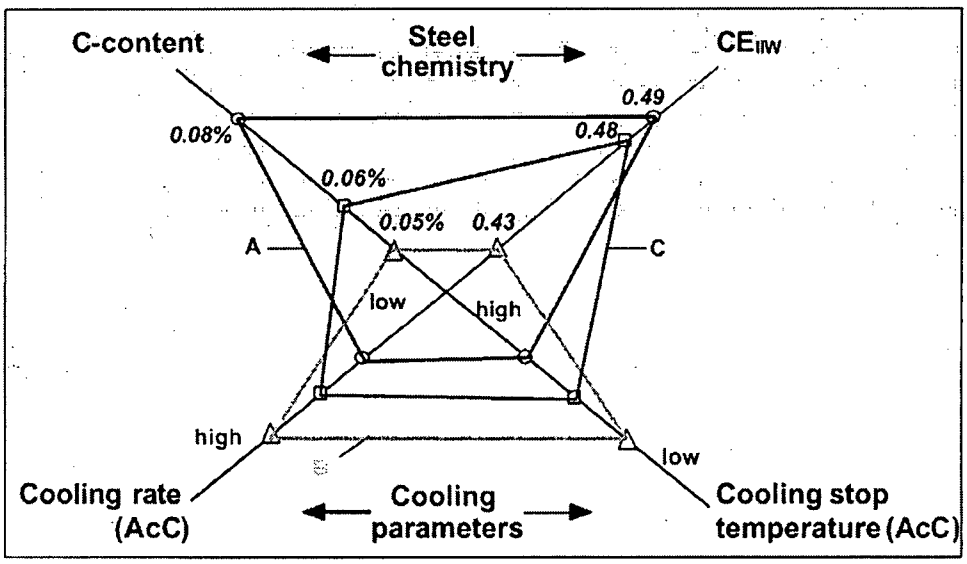

Figure 2.11 Modification of Steel Chemistry and Cooling Parameters to achieve the strength level of X-100 grade [71]

Approach A, which involves relatively high carbon content, has the disadvantage that the crack arrest toughness requirements to prevent long-running cracks, may not be fulfilled. Moreover, this approach is also detrimental, e.g. to field weldability.

Approach B, is practically similar to direct quenching with fast cooling rates down to a very low cooling stop temperature and hence results in the formation of uncontrolled fractions of martensite in the microstructure, which have a detrimental effect on toughness properties of base metal and leads additionally to the softening in the heat affected zone.

Experience gained meanwhile indicates that approach C is the best option. This approach enables the desired property profile to be attained through an optimized two-stage rolling process in conjunction with reduced carbon content, a relatively high carbon equivalent and optimized cooling conditions. The particular potential of the existing rolling and cooling facilities contributes significantly to the success of this approach.

Approach C, which involves a low carbon content, ensures excellent toughness as well as fully satisfactory field weldability, regardless of the relatively high carbon equivalent of the chemical composition. The chemical composition should therefore be considered acceptable for the purpose of current standardization.

CHAPTER THREE

3 Experimental Details

3.1 Specimen Preparation

Two API grades of HSLA pipeline steels were used as test materials in this study. The steel sheets of API X-80 and API X-100 grades were supplied by the CANMET Materials Laboratories. Several flat disc specimens were machined from the steels sheets with nominal dimensions of 14 mm diameter and 4 mm thickness.

In order to determine the chemical compositions (wt.%) of the specimens to be used in the experiments, two steel samples were submitted to the International Plasma Labs Limited (IPL) and they are shown in Table 3.1

Table 3.1 Chemical Compositions of API X-80 and API X-100 Steel Specimens (wt%)

Steel	C	Mn	Mo	Ni	Cu	Ti	V	Al	Cr	P	Fe
X-80	0.09	1.55	0.002	0.0001	0.0193	0.0461	0.0109	0.0363	0.022	0.0441	Bal.
X-100	0.07	2.19	0.2	0.1	0.3	0.01	0.0096	0.0257	0.02	0.0365	Bal.

Subsequently, an insulated copper connection wire was soldered to the back face of each test specimen, mounted then in a hard, cold-curing epoxy resin. To prevent the initiation of crevice corrosion between the epoxy and the specimen, the epoxy-specimen interface was masked with a solvent based insulating paint leaving a metal area of 0.1 cm^2 to contact the electrolyte.

Prior to each experiment, the working electrode surface was treated as follows:

- wet-ground to a 600-grit silicon carbide (SiC) finish
- degreased ultrasonically with acetone in bath of distilled water for 10 minutes
- rinsed with double distilled water
- dried in a stream of cool air
- finally immersed in the solution

3.2 Test Solutions

All solutions were prepared from distilled water and analytical-grade reagents. The sodium bicarbonate ($NaHCO_3$) solutions used in the tests varied from 0.01 M to 0.5 M with corresponding pH values in the range of 8.3 – 8.5.

Calculation according to the dissociation constants of H_2CO_3 showed that the concentrations of H_2CO_3 and CO_3^{2-} were only 1% of that of HCO_3^- with a solution pH

value range of 8.3 – 8.5. Therefore, it was acceptable that the concentrations of HCO_3^- during the experiments will be unchanged. The pH values were measured with a combination pH electrode (glass membrane with Ag/AgCl reference element) calibrated with pH value of 7.0 standard buffer solutions.

To investigate the effects of chloride ions (Cl^-) on pitting corrosion in bicarbonate solutions, Cl^- ions were added to the 0.5M $NaHCO_3$ solutions in the form of sodium chloride (NaCl) to yield concentrations of 0.001M, 0.005M and 0.01M. NaCl presence in the tested solutions did not shift the pH values outside the aforementioned range.

3.3 Electrochemical Cell Setup

Electrochemical testing was conducted in a standard glass cell containing the working electrode (specimen) and a graphite counter electrode figure 3.1. Potentials were measured with respect to an external Silver/Silver Chloride (Ag/AgCl) reference electrode interfaced to the test solution via a salt bridge assembly consisting of the test solution and a simulated Luggin-type polyethylene capillary that terminated ~ 2 mm from the specimen. A saturated potassium chloride (KCl) solution is associated with the reference electrode.

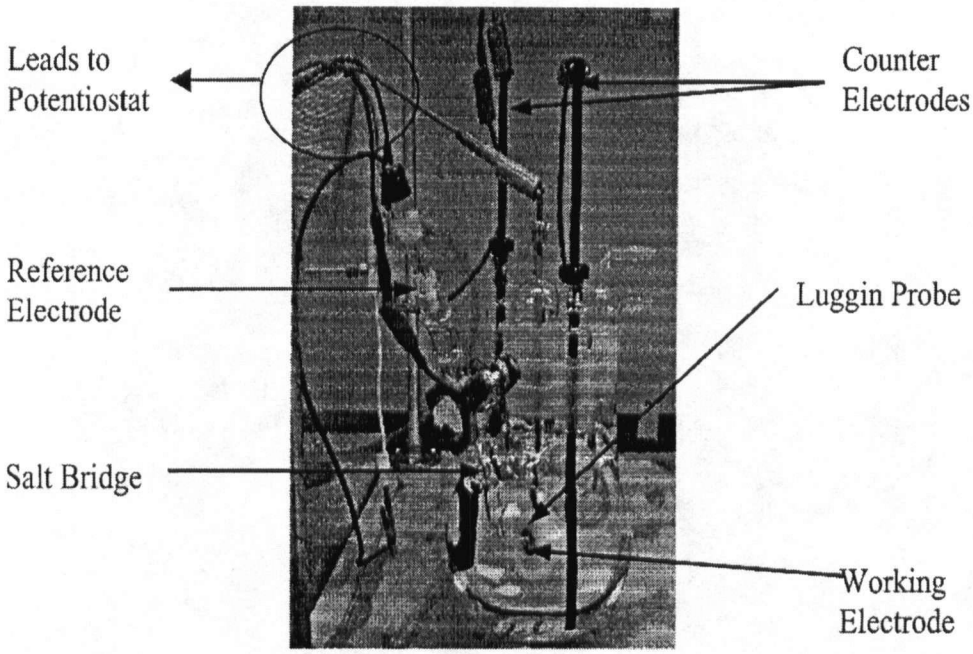

Figure 3.1 Standard Electrochemical Test Corrosion Cell

The potentiostat system utilized to perform and analyze the potentiodynamic polarization curves was Solarton Model (1286) with a software package having a combination of CorrWare (for hardware control and data acquisition) and CorrView (for data comparison and analysis).

The volume of the glass cell used in all experiments was approximately 600 ml of electrolytes where a fresh solution was utilized in every new test. To help minimize the concentration of dissolved oxygen, all test solutions were stirred magnetically and purged continuously with nitrogen for 30 minutes before each test. All experiments were conducted under ambient conditions with a temperature of ~ 22°C and a pressure of 1 atm.

Reproducibility was checked carefully by multiple runs (typically three identical runs) as in some experiments the effects described are quite small. For the polarization curves shown in this study, a large number of data points are displayed since the data were acquired at a rate of 5 points per mV.

3.4 Electrochemical Techniques

3.4.1 Open Circuit Potential Measurements

Open circuit potential measurements *(E_{op})* were made between the working specimen and the reference electrode without current being passed to the counter electrodes. This measurement showed the potential at which the anodic and cathodic reaction currents at the working electrode/ solution interface were balanced. In the case of corrosion of HSLA steels, these measurements are useful as qualitative information regarding the state of the working specimen surface.

E_{op} measurements were carried out prior to electrochemical polarization curve tests to ensure stability. They were also used to evaluate the effects of HCO_3^- inhibitors and relative nobility of the samples.

3.4.2 Potentiodynamic Curves

Potentiodynamic tests were carried out with a computer-controlled electrochemical interface (potentiostat), allowing continuous monitoring of potential *(E)*, total current *(I)*, and time *(t)*. Average current density *(i)* was obtained by dividing *(I)* by the initial working area of the specimen.

After allowing the specimen to attain a stable open circuit potential (*Eop*), the electrode potential was swept potentiodynamically at a rate of 1.0 mV/sec (unless otherwise indicated) from the initial potential of – 0.25 V versus *Eop* to the final potential of 1.6 V versus Ag/AgCl electrode. All potentials reported in this paper were measured with respect to Ag/AgCl electrode (E = 0.197 V vs. Standard Hydrogen Electrode SHE).

In this study, the potentiodynamic polarization curves were obtained for two different API grades of HSLA steels: X-80 and X-100. They allowed the determination of various regions of potential (anodic dissolution, pre-passivation, passivation, and trans-passivation) characteristics of each grade of tested steel.

The potential for stable pitting *(E_{pit})* was determined by noting the potential at which a sharp increase in the anodic current occurred, indicating sustained localized breakdown of the passive film of the tested material.

3.5 Materials Characterization

3.5.1 Scanning Electron Microscope (SEM) Observations

Pitting morphology features were examined by SEM using secondary electron imaging and 20 keV excitation. Quantitative observations included measurements of the average pitting density (number of pits/unit area) and their approximate diameters.

CHAPTER FOUR

4 Results and Discussion

4.1 Analysis of Microstructure

The addition of a small amount of alloying elements could significantly change the microstructure of HSLA steels used in the pipe-line applications. Consequently, this change in microstructure could modify to a big extent the mechanical properties of HSLA steels as well as their corrosion resistance. For this reason, two specimens of the as-received API X-80 and API X-100 steels were subjected to SEM examinations.

The specimens were firstly ground up to #1200 using SiC papers, degreased with acetone and then etched with a nital solution containing of 5% nitric acid (HNO_3) and ethanol (C_2H_5OH). The SEM pictures of the typical microstructures of API X-80 and API X-100 steels used during the experiments are presented in figure 4.1. The microstructure of API X-80 steel was mainly composed of pearlite and ferrite. There was also an indication of the presence of a small amount of bainitic structure. However, a predominantly martensitic structure with a lesser amount of bainite was detected on the specimen surface of API X-100 steel.

The steel chemistry (the alloying elements) variation between the two steels could be accounted to be one of the factors, in this case, affecting the significant change observed in the microstructures of API X-80 and API X-100 steels. The primary difference between API X-80 and API X-100 steels, with respect to their alloys, is the higher contents of molybdenum, copper, and nickel in API X-100 grade (Table 3.1). These alloying elements with the contents specified (table) could shift the pearlite transformation line of the continuous cooling transformation (CCT) diagram to its right and restrain the formation of ferrite but hardly retard the bainite and martensite transformations [67, 68].

Moreover, the addition of molybdenum, copper, and nickel in API X-100 steel could increase the temperature of the maximum rate of pearlite transformation and decrease the temperature of the maximum rate of bainite transformation. This would produce clearly a separation of the pearlite and bainite transformation lines and thus make the transformation of the pearlite/ferrite structure of API X-80 steel to the bainite/martensite structure of API X-100 steel easier even under the same cooling conditions [67, 68].

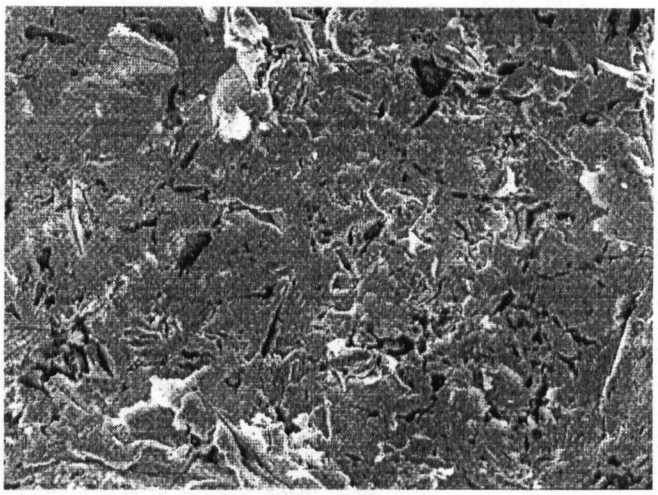

(a)

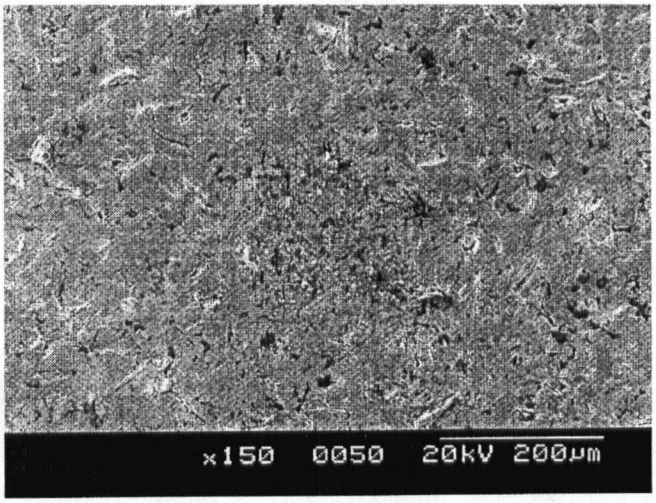

(b)

Figure 4.1 Typical microstructures of test materials under SEM (a) API X-80 steel and (b) API X-100 pipeline steel specimens used during the potentiodynamic polarization experiments

4.2 Open Circuit Potentials Behavior as a Function of Immersion Time

4.2.1 Effect of Bicarbonate Ions (HCO_3^-)

Open circuit potentials (*Eop*) of X-80 and X-100 steel specimens were followed over 1800 seconds in solutions of different HCO_3^- concentrations. Those are illustrated in figure 4.2 for both API X-80 and API X-100 steels. The general shape of the curves is the same for both steels in all HCO_3^- concentrations; *Eop* shifts continuously toward more negative values with increasing immersion time before it reaches the steady state. The steady state potential was reached in the first 1000 seconds or less for steel electrodes immersed in all solutions of bicarbonate ions.

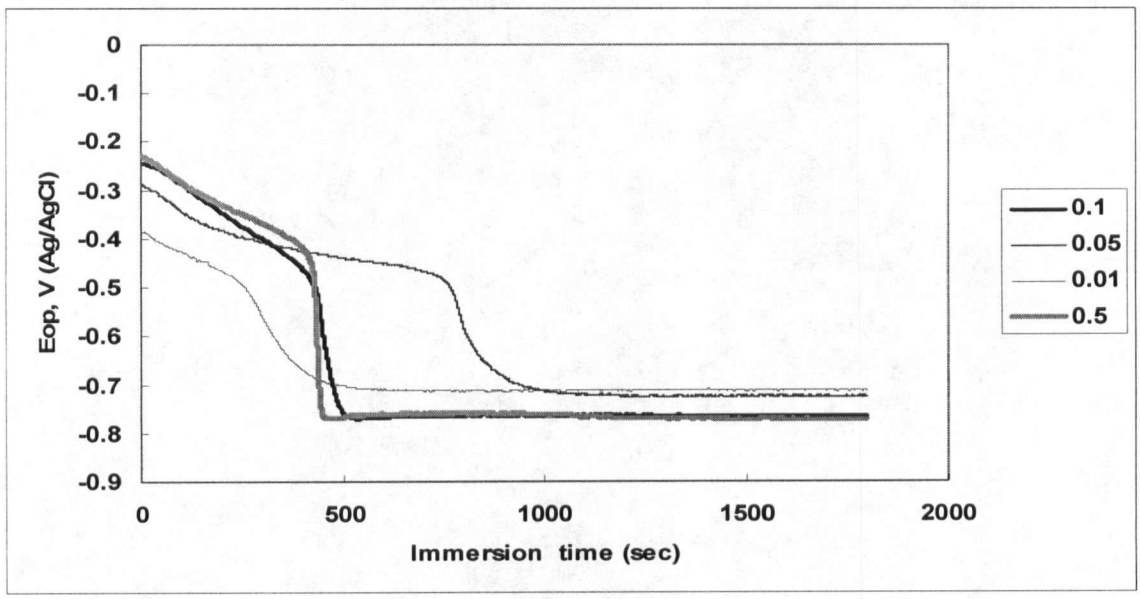

(a)

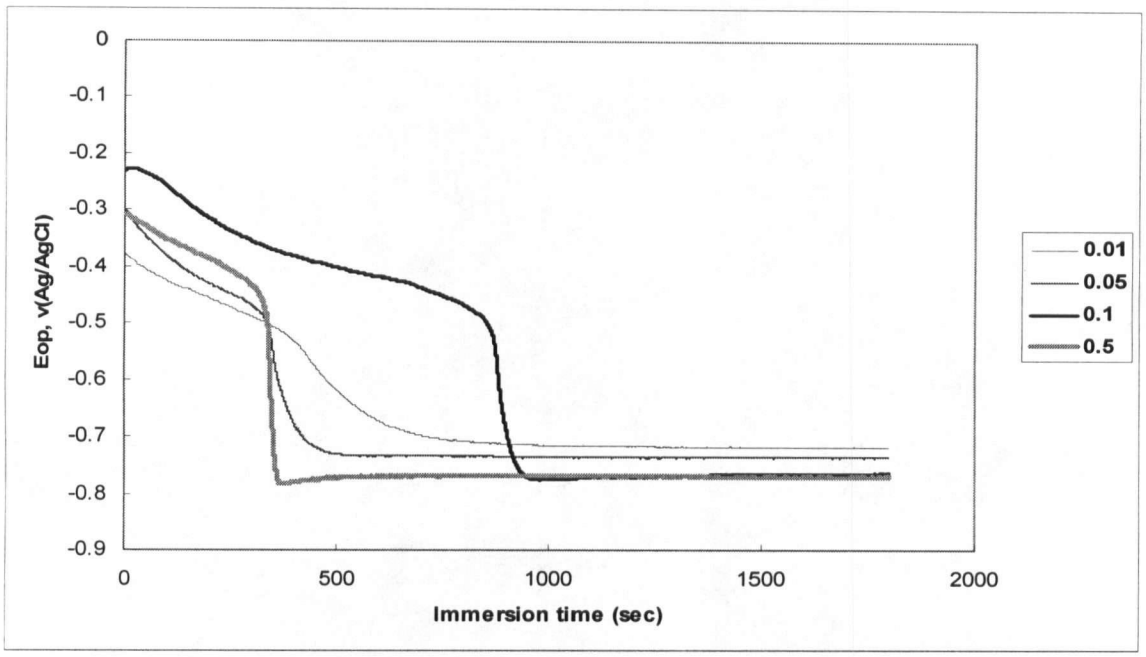

(b)

Figure 4.2 Open Circuit Potentials as a function of immersion time for tested API steels at various HCO_3^- concentrations [M]: (a) X-80 and (b) X-100

The steady state values of open circuit potentials, *Eop*, in various HCO_3^- concentrations for both API X-80 and API X-100 steels are summarized in table 4.1 and are sketched in figure 4.3. It is clearly seen that as the HCO_3^- concentration increased, *Eop* of API X-80 and API X-100 steels electrodes moved to a more negative value and thus this confirmed that the surfaces of steel specimens were able to form stable passive films more easily in relatively higher HCO_3^- solutions. Thus, the HCO_3^- ions can be considered as a typical example of its ability of passivating the HSLA steels based not on the conventional principle of retarding the electrochemical reactions but rather on the principle of enhancing the effectiveness of the cathodic process, i.e. by shifting the potential to a value at which formation of passivating film becomes possible.

Table 4.1 Open circuit potentials for API X-80 and API X-100 steels in various HCO_3^- concentrations

$[HCO_3^-]$ (M)	E_{op} (mV)	
	X-80	X-100
0.01	-714	-718
0.05	-726	-736
0.1	-765	-764
0.5	-773	-770

Even though both API X-80 and API X-100 steels shifted to more negative steady state E_{op} values with the increase in HCO_3^- concentrations, the closeness in the E_{op} steady state values of both steels at the same applied HCO_3^- concentration was also apparent. This might indicate that the alloy compositions and microstructures did play an analogous effect on the open circuit potentials of API X-80 and API X-100 steels at each applied HCO_3^- concentration.

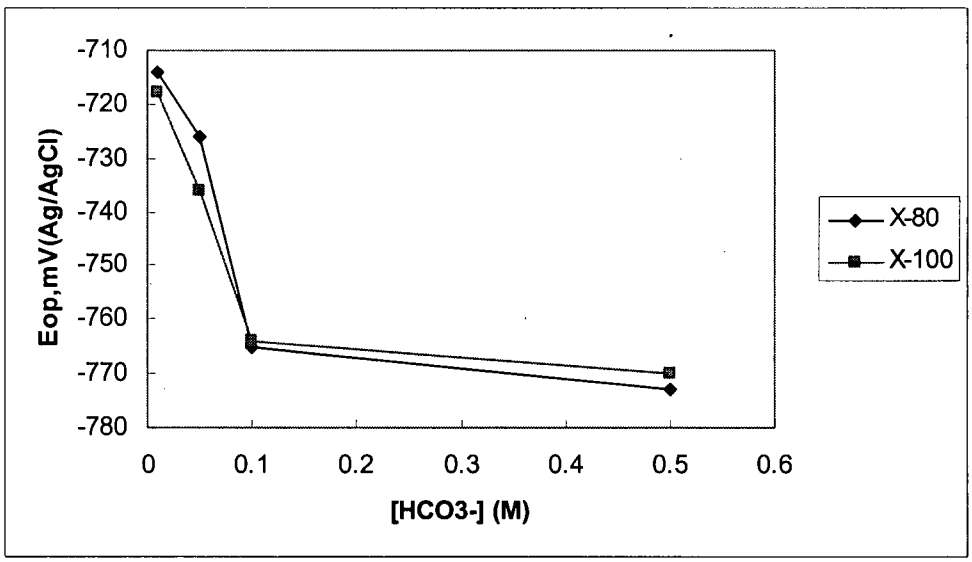

Figure 4.3 effects of HCO_3^- concentrations on open circuit potentials of X-80 & X-100 steels

4.2.2 Effect of Chloride Ions (Cl^-)

The behavior of the open circuit potentials (E_{op}) of API X-80 and API X-100 steel specimens at 0.5M HCO_3^- solution were studied with the presence of various concentrations of chloride ions from their initial immersion till they attained their E_{op} steady state values. The corresponding curves are illustrated in figure 4.4 for API X-80 and API X-100 steels. It is evident that the curves of both steels are similar with respect to their behaviors in the 0.5M HCO_3^- solutions without a remarkable influence of the chloride ion additives. The open circuit potentials (E_{op}) in the 0.5M HCO_3^- solution with the presence of different chloride ions concentrations also shifted to a more negative values and reached generally their steady state values within the first half of the immersion time displayed for the tests (1800 seconds).

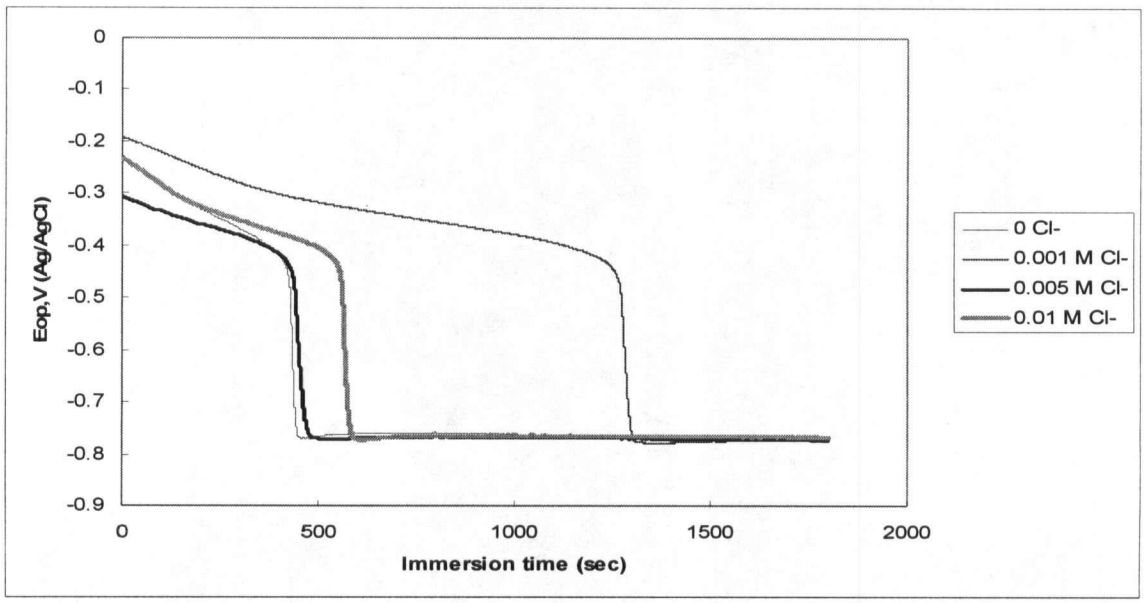

(a)

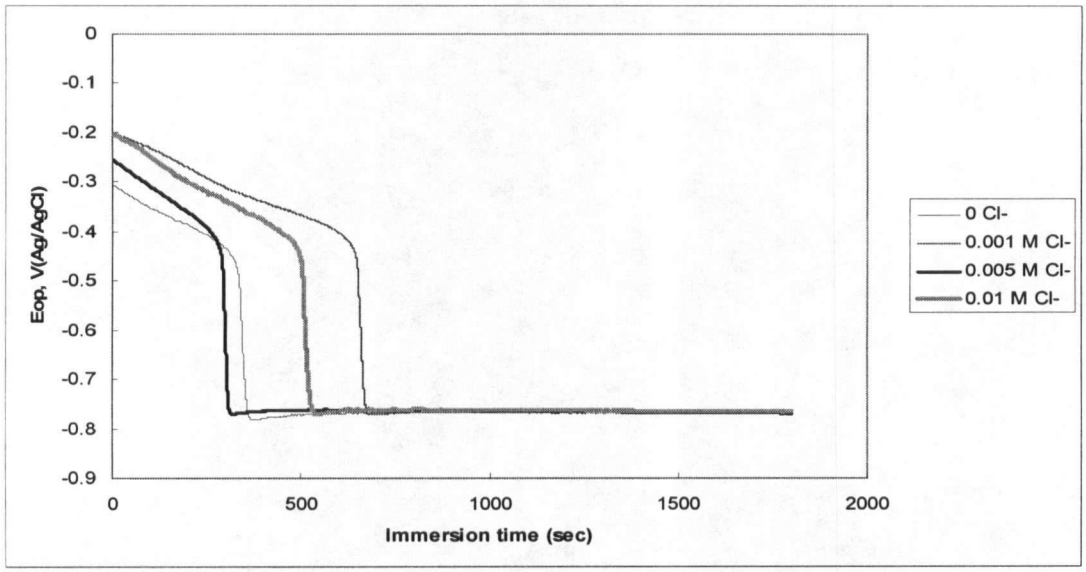

(b)

Figure 4.4 Open Circuit Potentials as a function of immersion time for tested API steels at various Cl^- concentrations: (a) X-80 and (b) X-100

Table 4.2 summarizes the steady state values of the open circuit potentials (E_{op}) in the 0.5M HCO_3^- solutions with the addition of various chloride ions for API X-80 and API X-100 steels. These values were obtained form figure 4.4. It is seen, evidently, that the E_{op} values of both steels shifted within a very narrow range of potentials despite of the significant increase in the chloride concentration.

Table 4.2 Open circuit potentials for API X-80 and API X-100 steels in 0.5M HCO_3^- solutions with various Cl^- concentrations

$[Cl^-]$ (M)	E_{op} (mV)	
	X-80	X-100
0	-773	-770
0.001	-776	-778
0.005	-772	-770
0.01	-767	-766

Moreover, it is clearly seen that as the chloride ions concentration increased in the test solution, the E_{op} moved to less negative values (figure 4.5) which is a fully contrary to the fact observed for the same steel electrodes in the free chloride ions solution and with the increase in HCO_3^- concentration. This may conclude that raising the chloride ions in 0.5M HCO_3^- solution could bring up the E_{op} to less negative values and thus narrowing or diminishing the passive layer formation on the surfaces of the steel specimens in the HCO_3^- solutions .

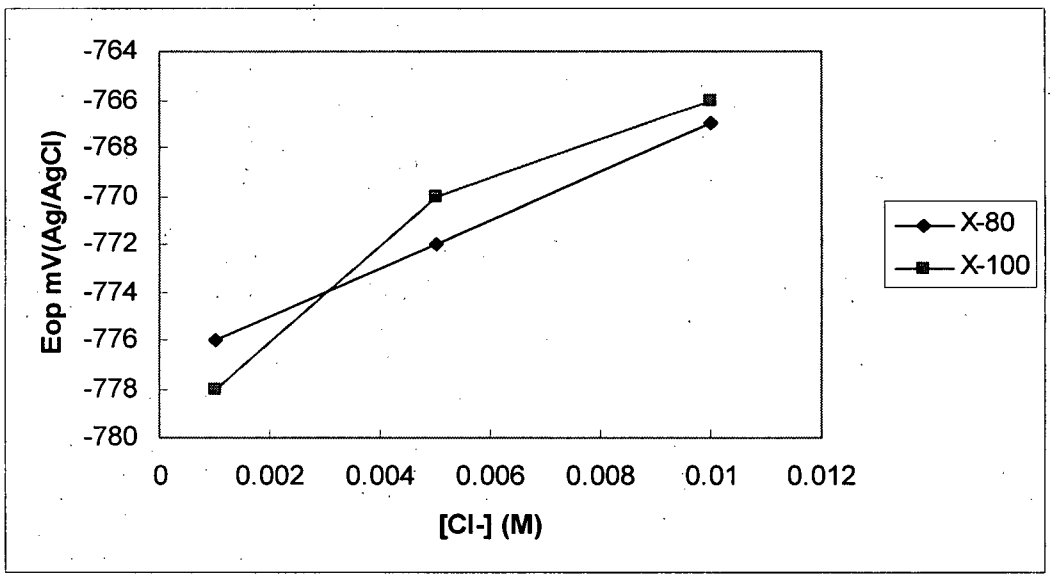

Figure 4.5 Effect of Cl^- concentrations on open circuit potentials of X-80 & X-100 steels

4.3 Potentiodynamic Polarization Curves

4.3.1 Effect of Bicarbonate Ions (HCO_3^-)

Figures 4.6 and 4.7 demonstrate the potentiodynamic polarization curves of API X-80 and API X-100 steels respectively in bicarbonate ions of various concentrations. Both steels showed very similar behaviors and they changed with the bicarbonate concentrations with respect to the number of oxidation (anodic) peaks. At the lowest HCO_3^- concentration (0.01M), one wide oxidation peak was observed at potentials of –2.7 and 96.5 mV for API X-80 and API X-100 steels respectively.

As the HCO_3^- concentration was increased to 0.05M, the aforementioned wide oxidation peak was broken up to a small peak followed by a larger one and the passivation potential became less noble and thus resulted in a wider passive region. A yellow to brown color film was produced on the surface of the subjected electrodes in the 0.01 and 0.05M bicarbonate solutions in the potential region just above the passivation potential, corresponding to the reduction in the anodic current density with the increase in potential

At 0.1M HCO_3^- test solutions, both steels illustrated two similar anodic peaks at approximately the same corrosion current density. The two anodic peaks were also apparent in 0.5M HCO_3^- solutions but the first peak occurred at a relatively higher

current density than at 0.1 M for both steels. A white film was formed on the surface of the steel electrodes in the 0.1 and 0.5M HCO_3^- solutions when the applied potential was increased to that corresponding to the oxidation current peak.

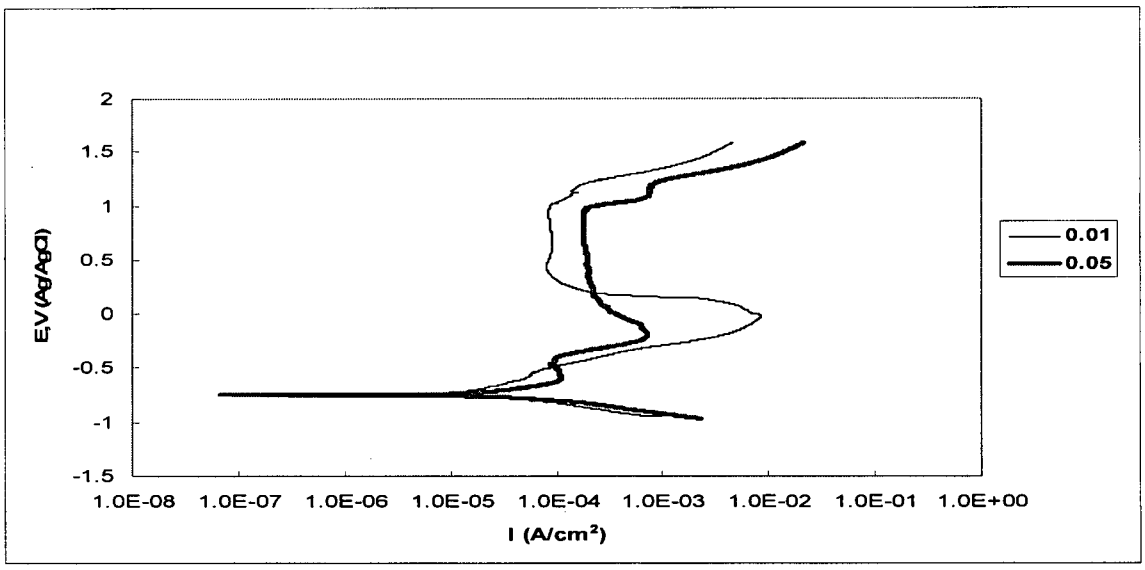

(a)

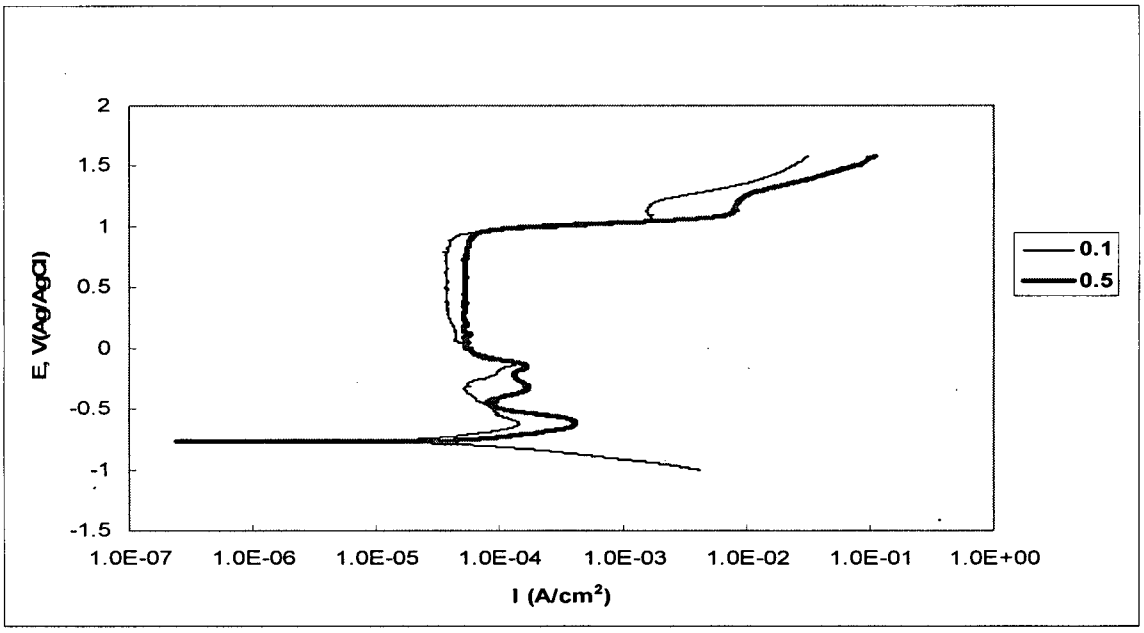

(b)

Figure 4.6 Potentiodynamic Polarization Curves for API X-80 steel in: (a) 0.01M and 0.05 M (b) 0.1 and 0.5M HCO_3^- solutions

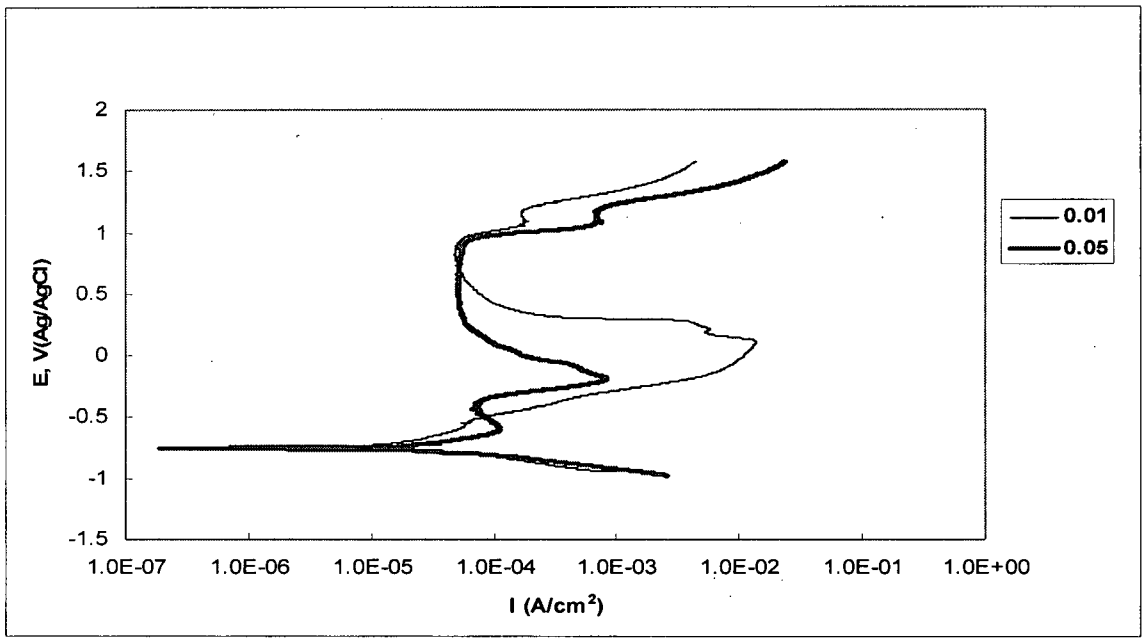

(a)

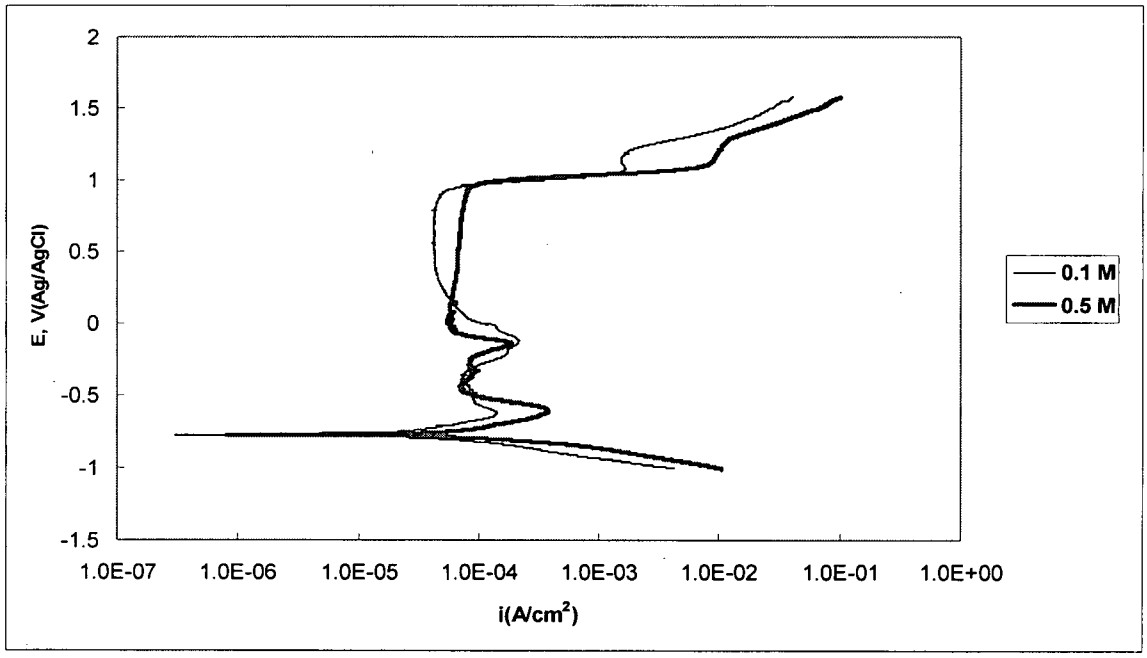

(b)

Figure 4.7 Potentiodynamic Polarization Curves for API X-100 steel in: (a) 0.01 and 0.05M (b) 0.1 and 0.5M HCO_3^- solutions

The several distinct characteristics exhibited by the polarization scans performed in various concentrations of HCO_3- solutions are investigated thoroughly in the following sections

4.3.1.1 The Active Dissolution Region

Electrochemical parameters of the active dissolution region, corrosion potential (*Ecorr*), corrosion current density (*Icorr*), anodic Tafel slope βa, and cathodic Tafel slope (βc) are reported in table 4.3. These parameters were calculated by Solarton Model (1286) and were confirmed by conventional method of manually drawing lines along the curves of the plots. This procedure is explained elsewhere [19]. The other parameters: *Epass*, *Ipass*, *ΔEpass*, *Epit*, which are shown in the following tables, were calculated from the excel plots of these curves to obtain the exact values.

Table 4.3 Electrochemical parameters of the active dissolution region for API X-80 and API X-100 steels in various HCO_3^- concentrations

Steel	$[HCO_3^-]$ (M)	*Ecorr* (mV)	*Icorr* (μA/cm²)	βa (mV/dec)	βc (mV/dec)
X-80	0.01	-746	24	545	128
	0.05	-748	35	277	111
	0.1	-774	45	284	103
	0.5	-775	120	261	109
X-100	0.01	-751	7	156	82
	0.05	-759	18	147	90
	0.1	-769	21	195	92
	0.5	-770	90	253	97

Figures 4.8 and 4.9 shows the relationship between the corrosion potential (*Ecorr*) and the corrosion current density (*Icorr*) with HCO_3^- concentrations respectively for API X-80 and API X-100 steels. As the bicarbonate concentration increased the corrosion potential for the steels decreased while the corrosion current density, measured by the Tafel extrapolation method, increased monotonically. In lower HCO_3^- solutions (0.01 & 0.05M), API X-80 showed higher corrosion potentials than API X-100, but the trend reversed in the higher HCO_3^- solutions (0.1 & 0.5M). In contrast, the corrosion current density was less in API X-100 compared to API X-80 in all HCO_3^- solutions.

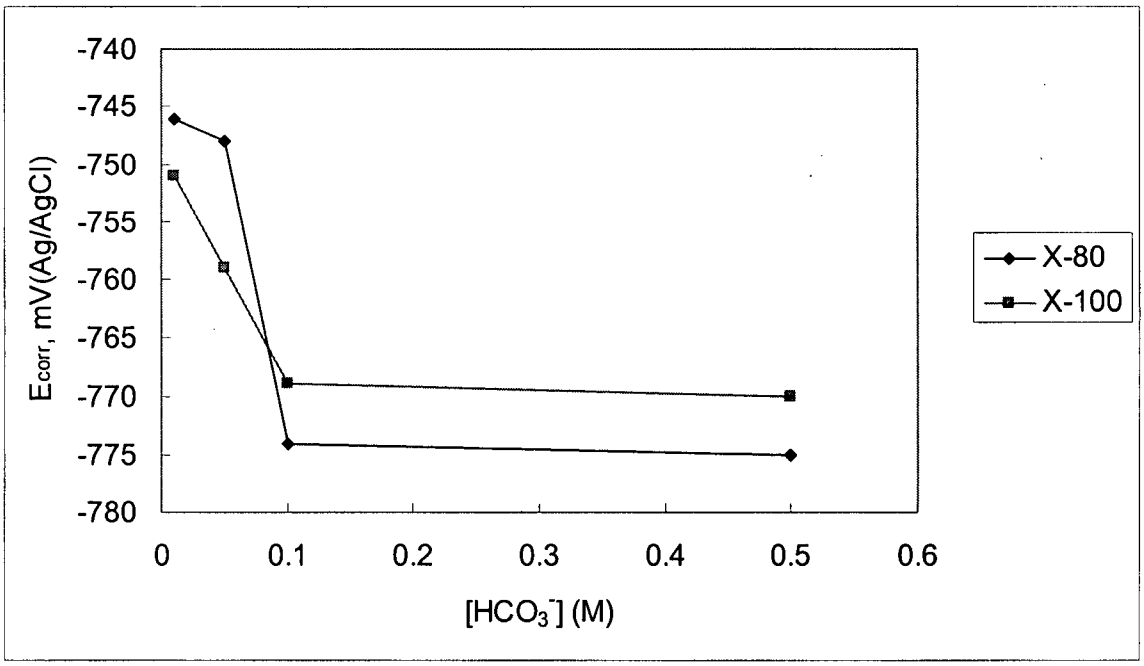

Figure 4.8 Effect of HCO_3^- concentrations on corrosion potentials of API X-80 & API X-100 steels

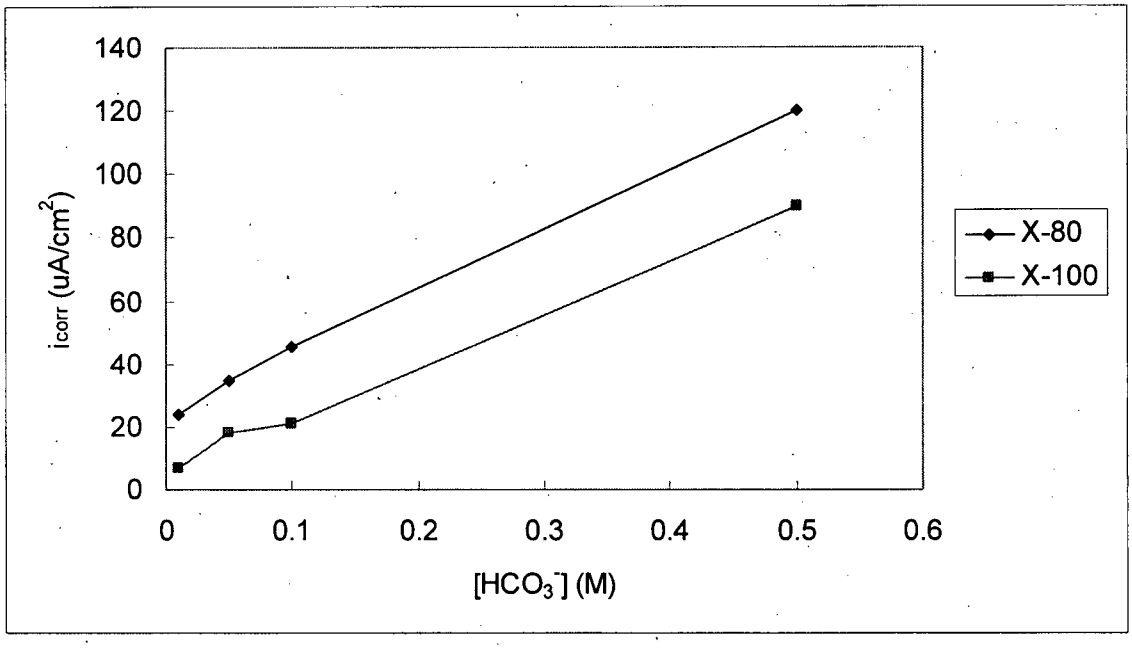

Figure 4.9 Effects of HCO_3^- concentrations on corrosion current densities of API X-80 & API X-100 steels

The corrosion rate values for X-80 and X-100 steels were calculated from the corrosion current densities based on Faraday's law in various concentrations of HCO_3^- ions and they are provided in table 4.4. The estimation of the corrosion rates by means of the Tafel extrapolation technique, within the active dissolution region, showed that X-100 steel had better corrosion resistance, by almost twice, than X-80 steel ones in all HCO_3^- test solutions (figure 4.10).

Table 4.4 Corrosion rates (mpy) for API X-80 and API X-100 steels in various HCO_3^- concentrations

Steel	$[HCO_3^-]$ (M)	*Icorr* ($\mu A/cm^2$)	Corrosion rate (mpy)
X-80	0.01	24	11
	0.05	35	16
	0.1	46	21
	0.5	120	55
X-100	0.01	7	3
	0.05	18	8
	0.1	21	9
	0.5	90	41

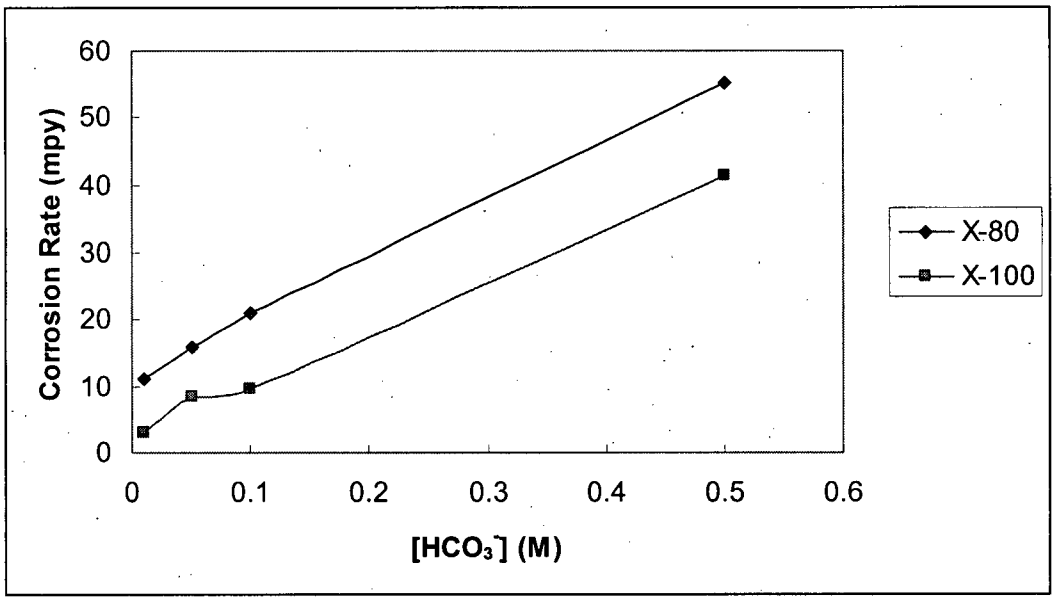

Figure 4.10 Corrosion rates of API X-80 and API X-100 steel specimens in different HCO_3^- solutions obtained by the polarization tests

4.3.1.2 The Passive Region

The electrochemical parameters of the passive region are reported in table 4.5. The primary passive potential (*Epass*), was measured in all experimental curves as the point at which the passive film starts to become stable (Point C, figure 2.3). The potential difference within the passive region (*ΔEpass*) was calculated as the breakdown potential (point F, figure 2.3) minus the primary passive potential (Point C, figure 2.3). The values of the passive current density (*Ipass*), which is a measure of the corrosion resistance of the steel specimen in the passive state, were obtained at a potential within the passive zone of the polarization curves of all tested steels.

Table 4.5 Electrochemical parameters of the passive region for API X-80 and API X-100 steels in various HCO_3^- concentrations

Steel	$[HCO_3^-]$ (M)	*Epass* (mV)	*Ipass* ($\mu A/cm^2$)	*ΔEpass* (mV)
X-80	0.01	600	79	371
	0.05	179	219	738
	0.1	74	38	813
	0.5	1	53	924
X-100	0.01	663	49	287
	0.05	320	55	565
	0.1	273	43	625
	0.5	6	68	922

An interesting fact between the potential difference within the passive region (*ΔEpass*) and the HCO_3^- concentration was seen for API X-80 and API X-100 steels (figure

4.11). It was found that the values of $\Delta Epass$ are directly proportional with the HCO_3^- concentration, i.e. as the HCO_3^- concentration increased in the test solution, the passive potential region was extended in width.

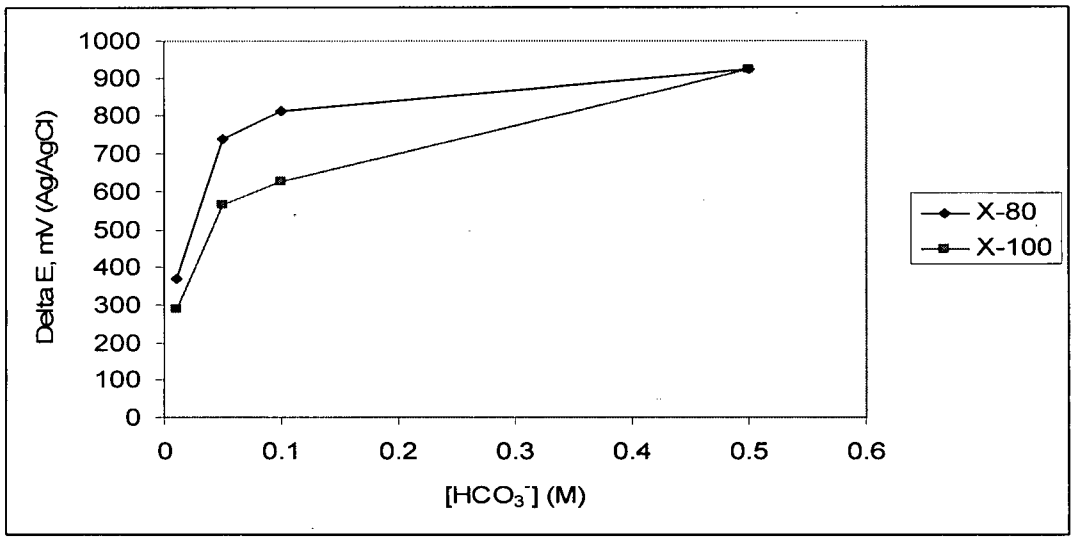

Figure 4.11 the passive potential region ($\Delta Epass$) of API X-80 and API X-100 steel electrodes in different HCO_3^- solutions

It was also noticed (figure 4.11) that the surfaces of API X-80 steel electrodes, particularly at low concentrations, had a more capability to widen the passive potential region than that of API X-100 steel specimens. The reason for this fact was not clear. It does suggest, however, that the intrinsic properties of the passive film are directly interrelated to the nature of the alloying elements, which will certainly alter the defect structure and vacancies in the films [72,73]. Another factor influencing the passive potential region variation between the API X-80 and API X-100 steels could be the change in the passive film thicknesses, according to the microstructure and alloy composition differences.

4.3.1.3 The Trans-Passive Region

The electrochemical behavior in this region is entirely attributed to the carbon steel dissolution by the formation of ferrite ions and oxygen evolution. The rate of diffusion of the dissolved species into the bulk solution is the rate-determining step [74]. Generally, the electrochemical dissolution is possible by a phenomenon known as trans-passivation. It occurs because in place of sparingly soluble oxides of lower valence produced at more positive potentials (i.e. Fe_2CO_3), which possess passivating properties, soluble FeO_4^{2-} oxide starts to form readily at a certain positive potential which does not posses protective properties. This leads to the disturbance of the passive state. The pitting potentials of both API X-80 and API X-100 steels in different concentrations of HCO_3^- solutions are illustrated in Table 4.6.

Table 4.6 Pitting potentials of API X-80 and API X-100 steels in various HCO_3^- concentrations

Steel	$[HCO_3^-]$ (M)	*Epit* (mV)
X-80	0.01	1001
	0.05	985
	0.1	NA*
	0.5	NA
X-100	0.01	970
	0.05	954
	0.1	NA
	0.5	NA

*NA: Not Applicable

Figures 4.12 and 4.13 show the SEM micrographs of API X-80 and API X-100 steels after potentiodynamic polarization with HCO_3^- concentrations of 0.01M, 0.05M, 0.1M, and 0.5 M respectively. The shape, size and density of the corrosion pits on the surface of API X-80 and API X-100 steel electrodes decreased with increasing the HCO_3^- concentrations. Pits did not form entirely in solutions of higher HCO_3^- concentrations (e.g. 0.1 and 0.5M). In contrast, API X-80 steels showed a more pitting density with uniform shape and small size whereas the pitting density formed on the surface of API X-100 steel electrodes was less but had a larger size and were inhomogeneous.

Solutions of low HCO_3^- concentrations (0.01 and 0.05M) resulted in a comparatively active primary passive potential and bigger size of pits, while solutions of higher HCO_3^- concentrations (0.1 and 0.5M) provided a more noble breakdown potential with no pits, which was attributed to the more stable passive film created on the steel specimen surfaces in higher HCO_3^- concentrations.

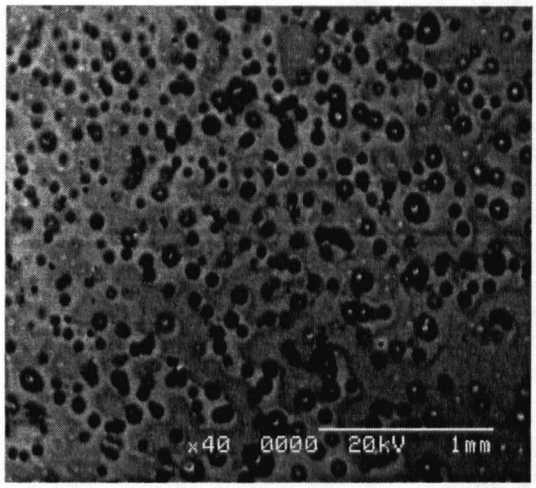

(a)

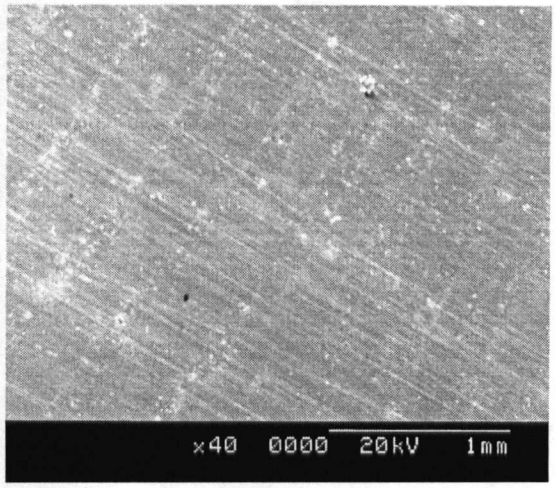

(b)

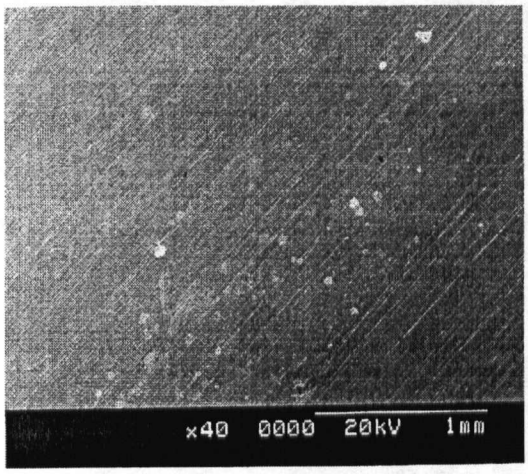

(c)

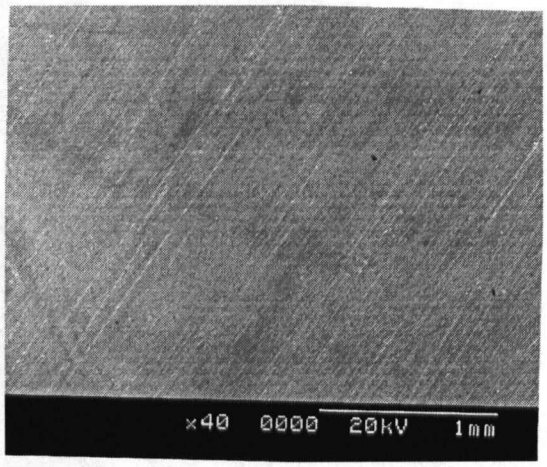

(d)

Figure 4.12 SEM micrographs of API X-80 steel after potentiodynamic polarization with HCO_3^- concentrations of: (a) 0.01M, (b) 0.05M, (c) 0.1M, and (d) 0.5M

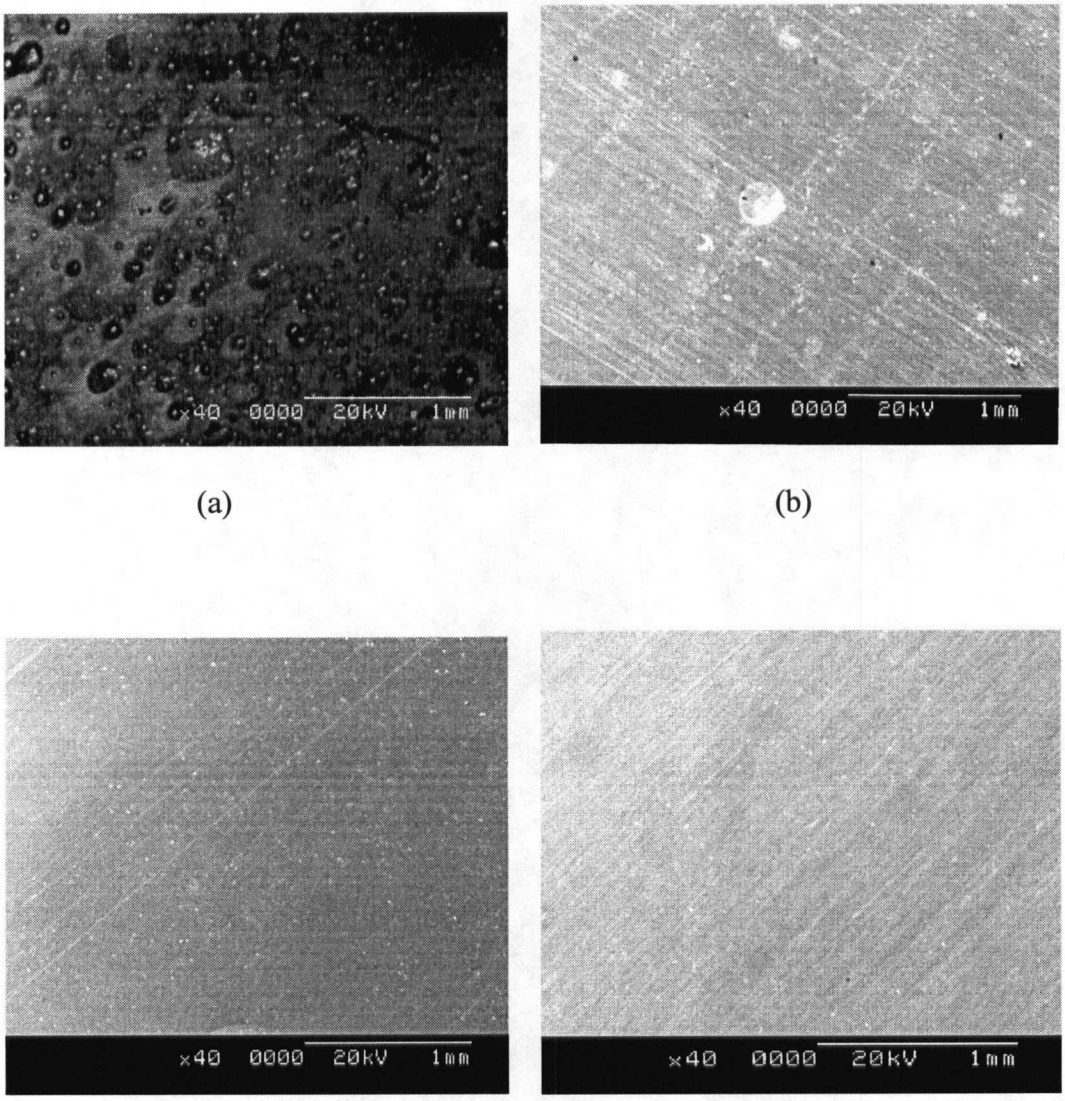

(a) (b)

(c) (d)

Figure 4.13 SEM micrographs of API X-100 steel after potentiodynamic polarization with HCO_3^- concentrations of: (a) 0.01M, (b) 0.05M, (c) 0.1M, and (d) 0.5M

It is generally recognized that the first stage in the anodic dissolution of carbon steel in oxygen-free HCO_3^- solutions is the equilibrium adsorption of OH^- with the formation of $Fe(OH)_{ads}$. Whether the adsorbed oxygen complex goes into solution or remains on the metal surface will depend on the potential of the electrode. For a positive shift in potential, it will be more likely that the complex will transform into an oxygen compound remaining on the metal surface and possessing good protective properties [75].

Moreover, the investigation revealed the presence of four distinctive anodic potential regions when the polarization is extended up to the oxygen evolution. These potential regions were identified and explained as follows [75]:

i. "Active region", associated with the formation of $Fe(OH)_{ads}$ and $Fe(OH)_2$.
ii. "Pre-passive region", associated with the formation of $HFeO_2^-$, FeO_2^{2-} and $Fe(OH)_2$ respectively.
iii. "Passive region", associated with the formation of $Fe_3O_4/\gamma\text{-}Fe_2O_3$
iv. "Trans-passive region", associated with the formation of $FeO4^{2-}$ and O_2

In this study, the shape of the potentiodynamic polarization curves for API X-80 and API X-100 steels showed identical behaviors and varied with the change of the HCO_3^- concentrations. At the lowest concentration of 0.01M HCO_3^- solutions used in the experiments, one wide anodic peak was observed on both steels. With the concentration increase to 0.05M, one small anodic peak followed by a larger anodic one appeared on

the curves. At a higher concentration (0.1M), two similar anodic peaks took place at approximately the same corrosion current density.

In 0.5M HCO_3^- solutions, there was a major anodic peak followed by two smaller peaks before reaching the passive region. The variation in the surface films formed on the steel electrodes was assumed to be the reason behind the dissimilar behavior of polarization curves. The corresponding potentials and corrosion current densities for all observed anodic peaks are presented in Table 4.7.

Table 4.7 potentials and corrosion current densities for the observed anodic peaks on the polarization curves for API X-80 and API X-100 steels

Steel grade	$[HCO_3^-]$ (M)	1st anodic peak		2nd anodic peak	
		E (mV)	*I* ($\mu A/cm^2$)	*E* (mV)	*I* ($\mu A/cm^2$)
X-80	0.01	-2.7	801	NA	*NA
	0.05	-606	111	-240	631
	0.1	-640	142	-141	127
	0.5	-637	401	-167	156
X-100	0.01	96.5	1353	*NA	*NA
	0.05	-625	101	-0.21	781
	0.1	-639	136	-131	213
	0.5	-616	368	-148	184

*NA: Not Applicable

The first anodic peak in all curves may be attributed to the first stages of steel electro-oxidization. Davies reported the formation of $FeCO_3$ film for pure iron in bicarbonate solutions (pH 8.8) by a dissolution-precipitation mechanism given below [76]:

$$Fe + 2H_2O \rightarrow Fe(OH)_2 + 2H^+ + 2e^- \quad (4.1)$$

$$Fe + HCO_3^- \rightarrow FeCO_3 + H^+ + 2e^- \quad (E^o = -716\ mV\ (Ag/AgCl)) \quad (4.2)$$

$$Fe(OH)_2 + HCO_3^- \rightarrow FeCO_3 + H_2O + OH^- \quad (4.3)$$

$$FeCO_3 + HCO_3^- \rightarrow Fe(CO_3)_2^{2-} + H^+ \quad (4.4)$$

In our case, the *Ecorr* was ranging from - 770 to - 746 mV (Ag/AgCl) in accordance with the bicarbonate concentrations used as test solutions. Those values obtained were close to the standard potential (E^o) from equation 4.2. This suggests that $FeCO_3$ formation is thermodynamically favorable.

The thermodynamics of equation 4.2 relies on the concentrations of hydrogen cation (H^+) or the hydroxide anion (OH^-) present in the environmental condition and particularly supported in solutions having high pH solutions. Since pH values of the HCO_3^- solutions fell within a narrow range of 8.3 to 8.5, no significant impacts of HCO_3^- concentration on this reaction were expected.

On the other hand, equation 4.3 is dependent on the pH value and the HCO_3^- concentration and is promoted by high HCO_3^- concentrations. As the HCO_3^-

concentrations were higher the corrosion current densities increased accordingly as illustrated in figure 4.9.

As a result, the reaction product formed on the steel surfaces in the active dissolution region is expected to be $FeCO_3$ as per the equation 4.3. The white-gray film observed on the specimens polarized in high concentration solutions of HCO_3^- (e.g., 0.5M) provided an apparent proof of $FeCO_3$ formation. Figure 4.14 shows the SEM images of surface films formed on the steel electrodes after potentiodynamic polarization in 0.5M HCO_3^- solutions.

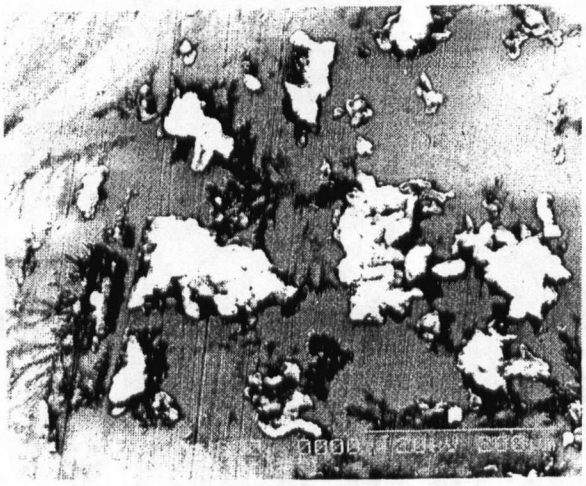

(a)

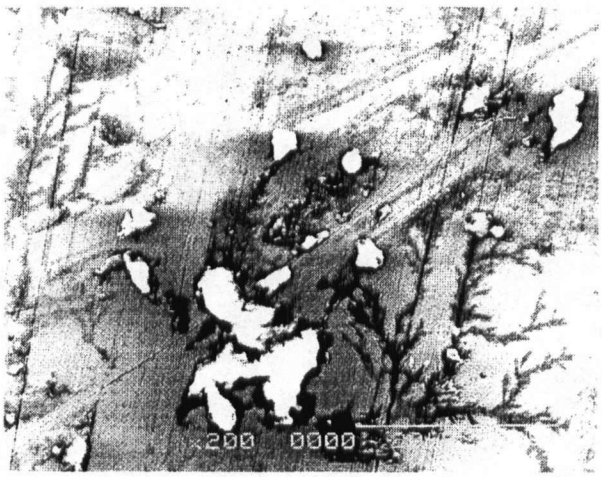

(b)

Figure 4.14 SEM images of surface films formed on the steel electrodes after potentiodynamic polarization in a 0.5M HCO_3^- concentration of steels: (a) API X-80 and (b) API X-100

Since the solubility product $FeCO_3$ is constant at a given temperature, increasing the HCO_3^- concentration not only made equation more favorable, but also made the saturation of $FeCO_3$ easier. From solubility data, a 1.6 x 10^{-9} M Fe^{2+} concentration is required for $FeCO_3$ to precipitate in a 1 M HCO_3^- solution. This will increase 100 times if the concentration of HCO_3^- is reduced from 1M to 0.01M. Therefore, when the HCO_3^- is reduced, the saturation of $FeCO_3$ is more difficult and hence the stability and the protectiveness of the $FeCO_3$ film decreases.

For the second anodic peak occurred in the polarization results for API X-80 and API X-100 steels with HCO_3^-, Thomas et al. observed similar second anodic peak in pure iron, at pH 11.3 that was attributed to the oxidation of $FeCO_3$ to a hydrated ferric oxide according to the following reaction [77]:

$$2FeCO_3 + 3H_2O \rightarrow Fe_2O_3 + CO_3^{2-} + 6H^+ + 2e^- \quad (4.5)$$

Jelinek et al. [78] reported observation of this second oxidization peak for mild steel in free oxygenated chloride solutions. It is also possible that the secondary anodic peak or repassivation at higher potential could also be due to the following reaction as proposed by Davies and Burstein for pure iron in bicarbonate solution at pH 8.8 [76]:

$$3Fe(OH)_2 \rightarrow Fe_3O_4 + 2H_2O + 2H^+ + 2e^- \quad (4.6)$$

In HCO_3^- solutions of lower concentrations, the $FeCO_3$ produced on the electrode surface of the steels due to the local saturation may have become unstable, e.g., $FeCO_3$ layer dissolved when the Fe^{2+} ions diffused away from the electrode surface and thus broke the local equilibrium of Fe^{2+} and CO_3^{2-} with $FeCO_3$ (equation 2.10). If this was the case, then the $FeCO_3$ film would have gone through a race between formation and dissolution processes. As a consequence, the polarization curves in low concentration HCO_3^- solutions showed a wide oxidation current peak of the highest current density. The increase in HCO_3^- concentrations resulted in lower primary passivation potentials *Epass* and hence to a gradual extension in the passivation layer ($\Delta Epass$) due to the increased stability of the Fe_2O_3 / Fe_3O_4 films.

4.3.2 Effect of Chloride Ions (Cl^-) Additives

The potentiodynamic polarization curves of API X-80 and API X-100 steels in 0.5M bicarbonate ions solutions of various chloride concentrations are illustrated in figure 4.15. The polarization curves distinctly changed with the addition of the chloride ions. The active dissolution, passive and trans-passive regions observed on the curves are discussed in detail in the following sections respectively.

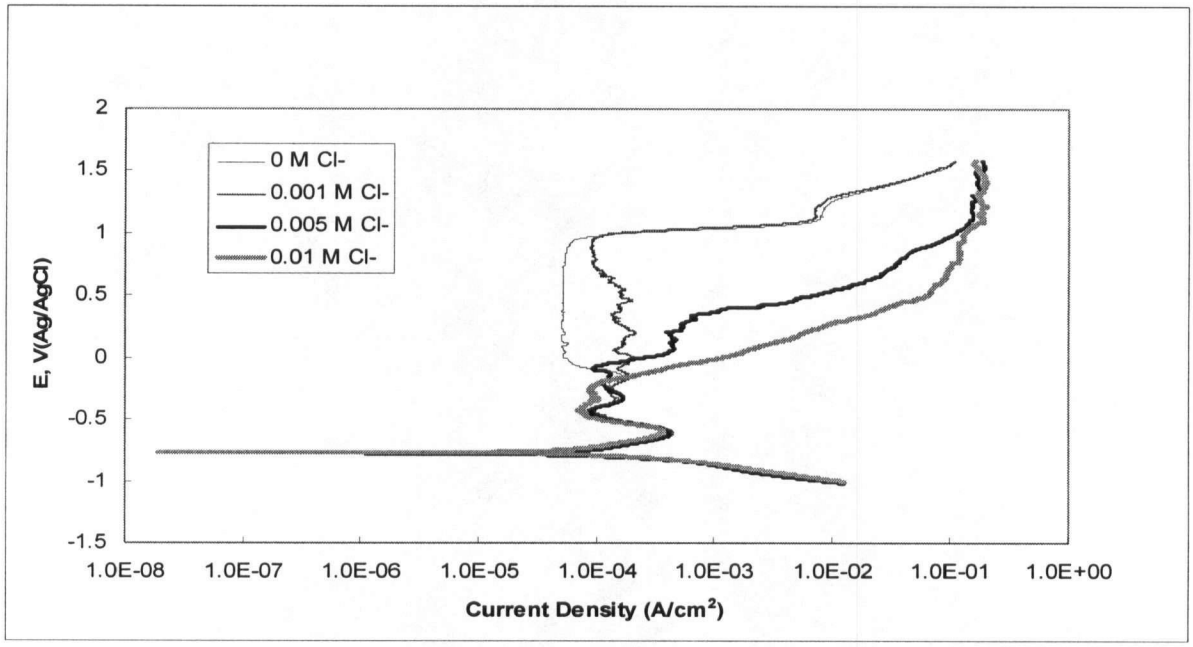

(a)

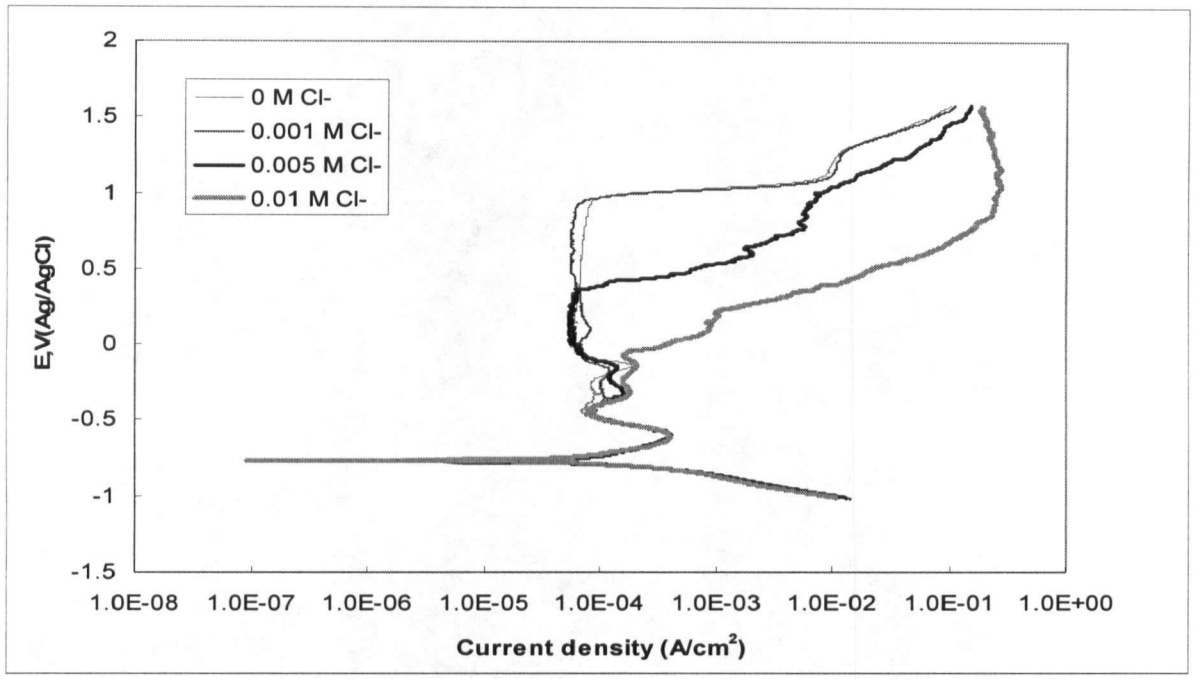

(b)

Figure 4.15 Potentiodynamic Polarization Curves for test steels at 0.5M HCO_3^- with various Cl^- concentrations: (a) API X-80 and (b) API X-100

4.3.2.1 The Active Dissolution Region

Table 4.8 summarizes the electrochemical parameters of the active dissolution region for X-80 and X-100 steels in 0.5M HCO_3^- with various concentrations of Cl^- ions: corrosion potential (*Ecorr*), corrosion current density (*Icorr*), anodic Tafel slope (βa), and cathodic Tafel slope (βc). Corrosion rates were also calculated for comparison and were included for both steels within the same table.

Table 4.8 Electrochemical parameters of the active dissolution region for API X-80 and API X-100 steels in 0.5M HCO_3^- and various Cl^- concentrations

Steel Grade	$[Cl^-]$ (M)	*Ecorr* (mV)	*Icorr* ($\mu A/cm^2$)	βa (mV/dec)	βc (mV/dec)	Corrosion rate(mpy)
X-80	0	-775	120	261	109	55
	0.001	-778	136	308	100	63
	0.005	-774	190	539	129	87
	0.01	-767	107	315	99	49
X-100	0	-770	90	253	97	41
	0.001	-783	133	353	99	61
	0.005	-771	147	408	110	68
	0.01	-766	40	132	82	18

The influence of the chloride ion is evident, since the Ecorr values are shifted first in the negative direction when 0.001M Cl^- is present in the 0.5M HCO_3^- solution and then move up in the positive trend when increasing the Cl^- concentrations to 0.005 and 0.01M respectively, as illustrated in figure 4.16. Additionally, the Icorr values are significantly changed with the addition of small amounts to the 0.5M HCO_3^- solutions and they showed a maximum at 0.005M Cl^- concentration (figure 4.17). Thus, a concentration of 0.001M Cl^- is able to make a remarkable change on the Ecorr and Icorr values, and accordingly on the corrosion rates of both API X-80 and API X-100 steels.

As in the HCO_3^- free chloride containing solutions, API X-100 steel specimens indicated better corrosion resistance with the presence of various concentrations of the

chloride ions than API X-80 steel specimens which is attributable to their higher degree of alloying elements, and thus different forms of microstructures.

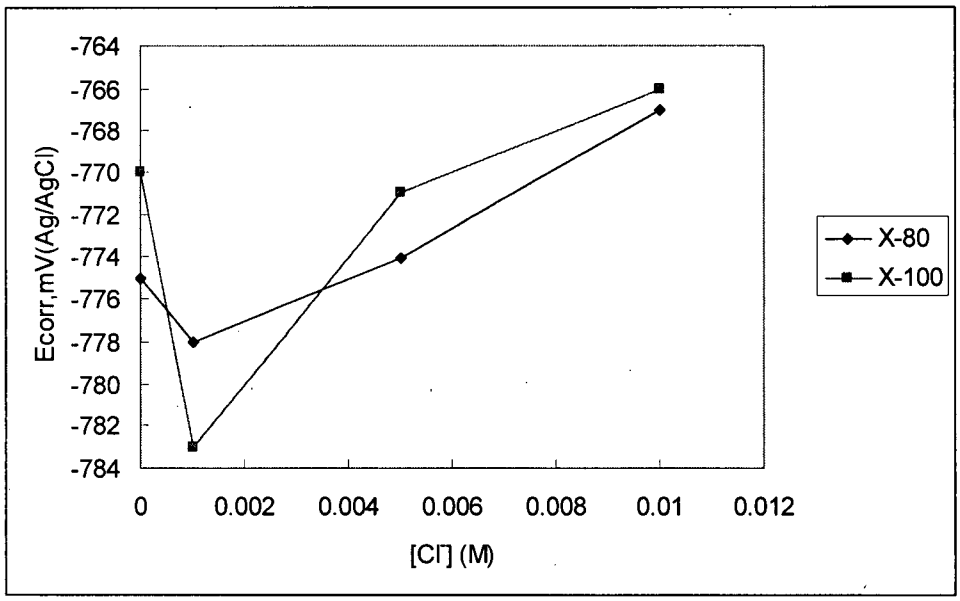

Figure 4.16 Effect of Cl^- concentrations on corrosion potentials of X-80 & X-100 steels in 0.5M HCO_3^- solutions

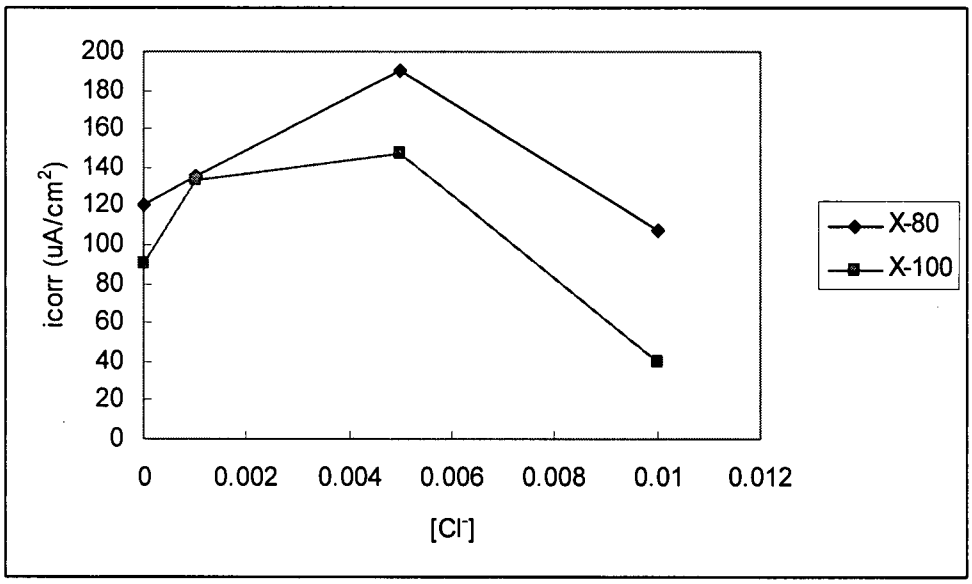

Figure 4.17 Effect of Cl^- concentrations on corrosion current densities of X-80 & X-100 steels in 0.5M HCO_3^- solutions

4.3.2.2 The Passive Region

The addition of small concentrations of the chloride ions to the 0.5 M HCO_3^- solutions had a major change on the polarization characteristics of API X-80 and X-100 steel electrodes and resulted in highly decreased passive potential regions. The passive films were easily ruptured and pitting corrosion took place faster. Besides, small variations in the current (noise) of amplitude of the order of few $\mu A/cm^2$ became more apparent as the chloride ion is increased in the solution. This is characteristic of metastable pitting, which often occurs at potentials less noble than the (phenomenological) measured pitting potential [79] and is associated with the formation of small (μm) metastable pits which is followed by rapid repassivation.

4.3.2.3 The Trans-Passive Region

The pitting potentials obtained from the curves as a function of the chloride ions are shown in table 4.10 for API X-80 and API X-100 steels. The pitting potentials were found to be very reproducible, most probably due to the fact that no crevices were observed on the surface of samples when checked under the microscope.

Table 4.9 Pitting corrosion potential of API X-80 and API X-100 steels in 0.5M HCO_3^- and various Cl^- concentrations

Steel	$[Cl^-]$ (M)	*Epit* (mV)
X-80	0.001	960
	0.005	-38
	0.01	-209
X-100	0.001	961
	0.005	372
	0.01	-35

The dependence of the pitting potential (E_{pit}) of steels on the concentration of the Cl^- anions can be seen more clearly in figure 4.18. It shows sigmoid curves including linear portions. These curves indicate that the presence of lower concentrations of the Cl^- (0.001M) anions has a slight effect on the value of pitting potential. This suggests that this lower concentration is not sufficient to cause the formation of active pits. The pits formed under these conditions are passive in nature.

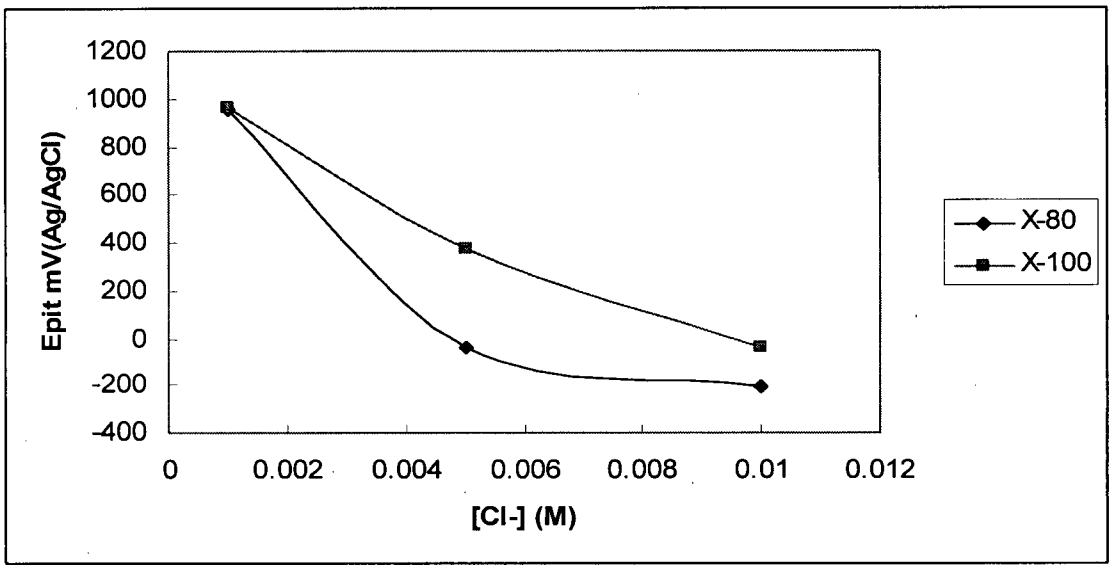

Figure 4.18 Effect of chloride concentrations on the pitting potentials of API X-80 & API X-100 steels in 0.5M HCO_3^- solutions

In a study related to the effect of the chloride ions on the pitting behavior of steels, Smialowska reported the existence of a linear relationship between pit nucleation potential and the chloride ion concentration according to the following equation [80]:

$$E_{pit} = a - b\,[Cl^-] \qquad (4.7)$$

If the difference between E_{pit} of API X-80 and API X-100 steels are compared, it was observed that of API X-100 steel was nearly 410 mV and 174 mV more noble than that of API X-80 steel at 0.005M and 0.01M Cl^- respectively.

It is known generally that the surface film formed on carbon steels in aqueous NaCl solutions containing HCO_3^- ions consists of many chemical species, such as Fe_2O_3, Fe_3O_4, $FeCO_3$, FeOOH, or green rust which is a hydroxyl complex involving both ferrous and ferric iron in addition to the Cl^- anion in the form of FeCl layer [40,41,42,43]. Among theses species, the FeCl layer formed by Cl^- anion adsorption is dissolved readily as $FeCl^+$ into aqueous Cl^- media via:

$$Fe + Cl^- = FeCl(ad) + e^- \qquad (4.8)$$

and:

$$FeCl(ad) = FeCl^+(aq) + e^- \qquad (4.9)$$

Where FeCl(ad) is an adsorbed species on the electrode surface and $FeCl^+(ad)$ is a species in an aqueous electrolyte [81]. Thus, the sites from which FeCl was detached acted as weak sites for the nucleation of pits in the surface film.

It could be concluded that if activating agent such as Cl^- anions is present in the electrolyte, then at some potential value the passive film is disturbed and breaks down and the process of anodic dissolution is accelerated. Moreover, complex halide possessing good solubility may also be formed. Pitting corrosion then sets in.

Therefore, it is possible to explain the general mechanism for the penetration, passivity, breakdown and pitting initiation that developed in the HSLA steel electrode by the chloride anions as follows: by virtue of its smaller size and larger polarizability, chloride anion becomes strongly adsorbed on the oxide film creating an electrostatic field accumulating Fe^{2+} in solution through the oxide film. The magnitude of the field depends upon the thickness of the oxide film as well as on the adsorbed negatively charged density.

The negatively charged density resulting from adsorption of the Cl^- anion can be expressed to create an equal and opposite charges on the metal side of the film. When this ultimately reaches a critical density, a local breakdown through the oxide film takes place allowing Cl^- anions to reach the bare metal causing onset of pitting corrosion initiation.

Figures 4.19 and 4.20 show SEM micrographs of pits formed on the surface of electrodes of API X-80 and API X-100 steels respectively after potentiodynamic polarization in free oxygenated 0.5M HCO_3^- with Cl^- concentrations of 0.001M, 0.005M, and 0.01M.

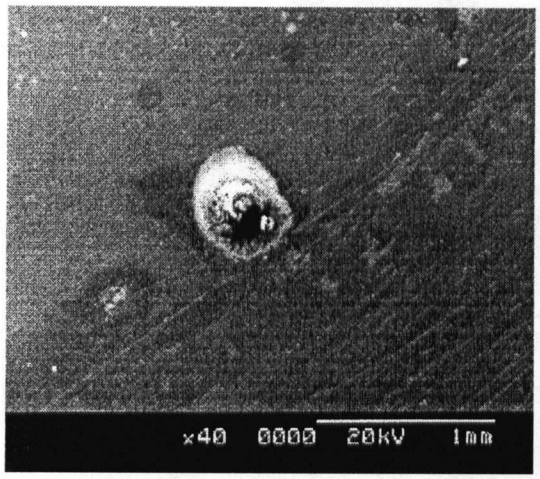

(a)

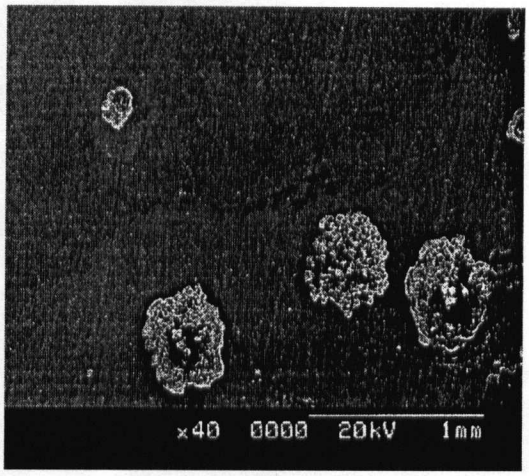

(b)

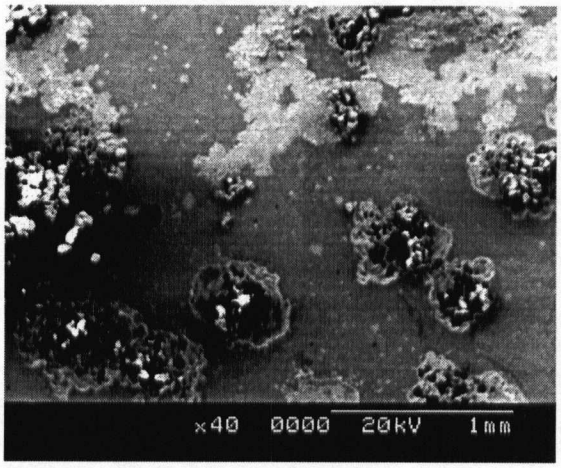

(c)

Figure 4.19 SEM micrographs of the pits formed on API X-80 steel after potentiodynamic polarization in free oxygenated 0.5M HCO_3^- with chloride ion concentrations of: (a) 0.001M, (b) 0.005M, and (c) 0.01M

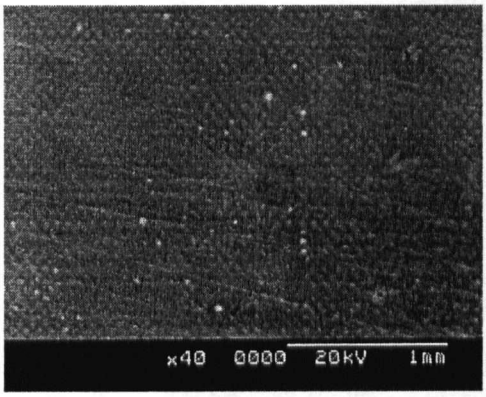

(a)

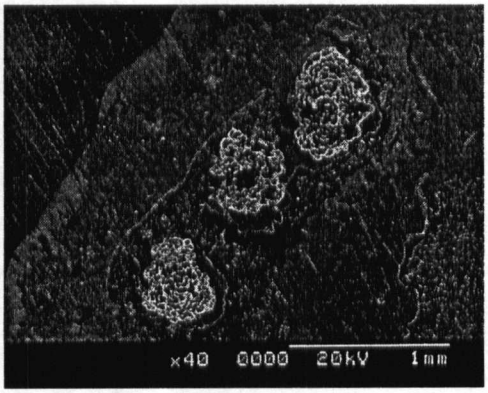

(b)

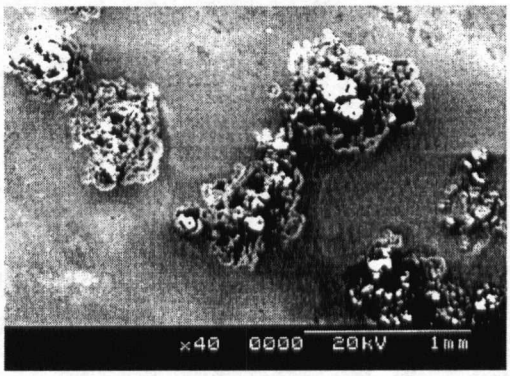

(c)

Figure 4.20 SEM micrographs of the pits formed on API X-100 steel after potentiodynamic polarization in free oxygenated 0.5M HCO_3^- with chloride concentrations of: (a) 0.001M, (b) 0.005M, and (c) 0.01M

The following Table 4.11 summarizes changes in the pit number density and the average diameter as obtained by SEM technique for both API X-80 and API X-100 steels. The SEM pit number density was measured by counting the number of pits on the surface of the electrodes.

Table 4.10 Average Pit Diameter (d_{pit}) and Pit Number Density (ρ_{pit})

Steel	[Cl^-] (M)	d_{pit} (μm)	ρ_{pit} (pits/cm^2)	Remarks
X-80	0.001	37	6	Small and open pits
	0.005	76	47	Small and open pits
	0.01	76	67	Small and open pits
X-100	0.001	17	2	Small pits
	0.005	76	21	Small and open pits
	0.01	195	36	Larger pits, two or three pits joined

As it is illustrated in the table, the pit number density on both steels increased as the Cl^- anions increased from 0.001 to 0.01M but it was always less for API X-100 steel. The pits shape and average diameter was almost similar on API X-80 and API X-100 steels on 0.001 and 0.005M NaCl. At the former concentrations, the steels exhibited large numbers of very small open pits with a hemispherical morphology shape of an average diameter of ~ 76 μm.

On the other hand, the appearance and distribution of pits slightly differed between API X-80 and API X-100 steel surfaces as the Cl^- anions increased to 0.01M. With a lesser pit number density, the average pit diameter formed on API X-100 electrode surfaces became larger (~ 195 μm) and the joining of two or three pits were also observed. In contrast, API X-80 steels specimens showed a larger pitting density with approximately the same average diameter of pits obtained at 0.001 and 0.005M NaCl.

4.3.3 Comparative Remarks on the Corrosion Behavior

API X-100 steel revealed to have a lower corrosion rate in the active dissolution region than X-80 steel in all test solutions containing HCO_3^- ions with or without the presence of Cl^- ions. The main cause for the differences in the corrosion characteristics between API X-80 and API X-100 steels in the active dissolution region obtained under the same experimental conditions may have resulted from the noticeable variance in the alloying contents with respect to the molybdenum, copper and nickel and thus in the different microstructure formed for both steels. The chemical analysis indicated that API X-100 had a higher alloying addition in the mentioned elements than for API X-80 steel.

It was found that when Cu is present as an alloying element in low carbon steels with a minimum of 0.1%, it could form copper oxides in the corrosion product layer in

solutions containing HCO_3^- and Cl^- ions and thus could promote a more protective film on the steel surface [80]. Because Cu is less soluble than Fe, the amount of the insoluble oxides in low alloy steels was larger than the amount of dissolved oxides in plain carbon steels. The dissolution process leads to enrichment of Cu in the corrosion product formed on the surface of the steels. Accordingly, API X-100 steel specimens had more protective, thick corrosion product films than API X-80 steel ones. In similar results, David et al. [83] found that Mo, Cu, Ni additions to API X-80 steel in a test solution consisting of a mixture of NaCl and $NaHCO_3$ reduced its corrosion rates and the same author in a different study [82] demonstrated that Mo and Cu additions to API X-70 steels were beneficial in the corrosion rate reduction with the same previous solutions.

Although a quite number of studies agreed on the positive influence of Ni addition on the corrosion behavior of low alloy carbon steels [82,83,85], very few research addressed the hypothetical mechanisms by which the Ni content could improve their corrosion resistance in solutions containing Cl^- ions. In a previous study, Toshiyasu et al. [86] analyzed the corrosion product formed on low alloy steels in 0.5% wt. NaCl solutions by the means of Transmission Electron Microscopy (TEM) and X-ray Photoelectron Spectroscopy (XPS) techniques. He found that Ni was involved in the formation of Fe_3O_4 in the corrosion product layer and helped to convert the layer into a dense and fine structure and thus this structure could prevent the penetration of Cl^- ions and effectively decrease the corrosion of the steels.

The improvement in the pitting corrosion resistance of API X-100 steel with the higher additions of Mo, Cu and Ni in the trans-passive region than those predicted for API X-80 steel may reflect chemical or physical changes that produce increased resistance because initiation is inhibited or because pits repassivate more readily. In this study, Mo could be considered as the most significant alloying element that improved the pitting corrosion resistance of API X-100 steels compared to API X-80 grades. Taking into account the electrochemistry of Mo, it becomes evident that Mo can dissolve at relatively low potentials due to the formation of soluble MoO_4^{2-} species [16]. The potential region for this reaction is situated in the passive region of Fe based alloys.

As a result, dissolved Mo species may have played a crucial role on extending the pitting potentials to more noble values of API X-100 steel specimens in electrolytes containing Cl^- ions by the formation of a more protective and stable salt layer, properly composing of $FeMoO_4$. Also in case of pure Fe, a positive impact on MoO_4^{2-} in neutral solutions on the pitting resistance of Fe has been reported [87]. In binary Fe/Mo alloys, alloyed Mo was found to increase the resistance to pitting in neutral solutions containing Cl^- solutions [88]. It was suggested that the better corrosion resistance due to adding Mo reflects a decrease in the dissolution rates in the concentrated solution within the pit [88]. Mo is considered to adsorb at the dissolving interface, so inhibiting the dissolution kinetics [89].

CHAPTER FIVE

5 Conclusions and Recommendations

Studies on the newer generation of HSLA pipeline steels, API X-80 and X-100 grades, were performed by means of open circuit potentials (E_{op}), potentiodynamic scans, and SEM experiments in free oxygenated bicarbonate/chloride media. On the basis of the results of the present study, the following conclusions could be drawn:

- As the HCO_3^- concentration increased, E_{op} of API X-80 and X-100 steels shifted to more negative values and thus leading to widen the passive region. This also confirmed that the surfaces of steels were able to form more easily stable passive films in relatively higher HCO_3^- concentrations. The addition of small amounts of Cl^- ions in 0.5M HCO_3^- solutions moved E_{op} up to less negative values, evidencing their ability to narrowing or even diminishing the passive layer formation on the surface of the steels
- Both API X-80 and API X-100 steels revealed identical polarization behaviors with respect to the shape of the oxidation peaks. However, the number of the oxidation peaks varied with the HCO_3^- concentration in the test solutions.
- The potential difference within the passive region (ΔE_{pass}) was found to increase with increasing the HCO_3^- concentration in the test solutions and thus extended the passive potential region in width. In contrast, the addition of the Cl^- ions

significantly lowered the passivation tendency of the steels in the HCO_3^- solutions

- The estimation of the corrosion rates by means of the Tafel extrapolation method showed that API X-100 steels had better corrosion resistance, by almost double, than API X-80 steels in HCO_3^- solutions with or without the presence of Cl^- ions. The addition of the Cl^- ions, however, increased generally the corrosion rates for both steels. Furthermore, API X-100 steel resulted in higher positive pitting potentials and consequently better pitting corrosion resistance than API X-80 steel for the range of Cl^- concentrations investigated
- SEM observation indicated that solutions of low HCO_3^- concentrations (0.01 and 0.05M) resulted in a comparatively active primary passive potential and bigger size of pits, while solutions of higher HCO_3^- concentrations (0.1 and 0.5M) provided a more noble breakdown potential with no pits, which was attributed to the more stable passive film created on the steel specimen surfaces in the higher HCO_3^- concentrations. On the other hand, pit morphology as examined under the SEM technique for 0.5M HCO_3^- solutions containing various concentrations of Cl^- ions indicated that the density and the diameter of the stable corrosion pits increased with increasing the Cl^- concentration in the test solutions
- The lower corrosion rates and the better pitting corrosion resistance for API X-100 steel compared to API X-80 steel may have resulted form the visible variance in the alloying contents with respect to the molybdenum, copper and nickel elements and thus in the different microstructure formed for both steels.

This, in turn, could make a change in the thickness and the protectiveness of the passive films formed on the surfaces of the steels.

To further address the present study, the following recommendations may be offered:

- The effect of higher temperatures on the corrosion and passivation behavior should be investigated for the tested HSLA steels.
- As the greatest susceptibility to SCC has been correlated with potentials observed in the active/passive transition state, a closer link could be established between the current results and the SCC phenomena by performing a series of SSRT tests.
- The influence of the pH factor should be investigated to cover a wider range of values on the electrochemical behavior of the tested HSLA steels.
- Further work should be carried out into the role and the mechanism by which Ni and Cu elements could help improve the corrosion rates of the HSLA steels.
- Many publications that discuss pipeline steels residing in neutral aqueous media have shown that the hydrogen ingress play a considerable role during the process of SCC. Therefore, the hydrogen influence on the corrosion polarization behavior is worthwhile to be explored.

NOMENCLATURE

API	*American Petroleum Institute*
Ag/AgCl	*Silver/Silver Chloride Reference Electrode*
B_a	*Anodic Tafel Slope*
B_c	*Cathodic Tafel Slope*
CANMET	*Canadian Centre for Mineral and Energy Technology*
CCT	*Continuous Cooling Transformation*
d_{pit}	*Average Pit Diameter*
ρ_{pit}	*Pit Number Density*
e^-	*Electron*
E	*Potential (Volt)*
E_{corr}	*Stable Active State Dissolution Potential*
E_{op}	*Open Circuit Potential*
E^o	*Standard Reduction Potential*
E_{pass}	*Primary Passivation Potential*
ΔE_{pass}	*Potential Difference in the passive region*
E_{pit}	*Pitting Potential*
EDX	*Electron Dispersive X-ray*
HIC	*Hydrogen Induced Cracking*
HSLA	*High Strength Low Alloy*
IGSCC	*Intergranular Stress Corrosion Cracking*
I_{corr}	*Corrosion Current Density (A/cm^2)*
I_{pass}	*Passive Current*
M	*Molar (mole/Liter)*
mpy	*Mills per year*
N	*Normal*
SCC	*Stress Corrosion Cracking*
SEM	*Scanning Electron Microscopy*
SHE	*Standard Hydrogen Electrode*
SRET	*Scanning Reference electrode Technique*
SSC	*Sulfide Stress Cracking*
SSRT	*Slow Strain Rate Test*
TEM	*Transmission Electron Microscopy*
TGSCC	*Transgranular Stress Corrosion Cracking*
um or μm	*Micrometer (1.10^{-6} meter)*
XRD	*X-Ray Diffraction*
XPS	*X-Ray Photoelectron Spectroscopy*
Wt.%	*Weight %*

References

[1] Arieta FG, Sellars CM. The Minerals, Metals and Materials Society, 1993. p. 101.

[2] ASM Committee on Carbon and Alloy Steels. ASM Metals Handbook, vol. 3. 9th Edition. 1980, p. 3.

[3] Andews R. M., Batte A. D., "Developments in Fracture Control Technology for Gas Pipelines Utilizing High Strength Steels", Advantica, Loughborough, UK, 2001

[4] Espiner R., "Update from BP's Pipeline Cost Reduction Technology Project", Proceedings of Onshore Pipelines Conf., Dec. 2002, p. 28.

[5] Fairchild, D. et al. "High Strength Steels – beyond X-80", Proceedings of Application and Evaluation of High Grade Linepipe in Hostile Enlivenments Conf., Yokohama Nov.2002, p. 307.

[6] Glover, A. "Application of Grade 555(X-80 and 690(X-100) in Arctic Climates", Proceedings of Application and Evaluation of High Grade in Hostile Environments Conf., Yokohama Nov.2002, p. 33.

[7] Barsanti, L at al. "From X-80 to X-100: Know-How Reached by ENI Group on High Strength Steel", Proceedings of Application and Evaluation of High Grade in Hostile Environments Conf., Yokohama Nov.2002, p. 33.

[8] Update Online Magazine, March, 2004, Vol. 4, Issue 2, http://www.transcanada.com

[9] Lopez. H. F., "Effect of Heat Treatment on the Stress Corrosion Resistance of a Micro-Alloyed Pipeline Steel", Corrosion Science 41, 1999, p. 1037-1049

[10] Gu B., Yu W., Lou J., Mao X., " Transgranular Stress Corrosion Cracking of X-80 and X-52 Pipeline Steels in Dilute Aqueous Solution with Near-Neutral pH", corrosion, March, 1999

[11] Lu B, Luo J., "Effect of Microstructure on Near-Neutral pH SCC Resistance of Pipeline Steels", The Metallurgical Society of CIM, August, 2003.

[12] Koh S., Yang B., Kim K., "Effect of Alloying Elements on the Susceptibility to Sulfide Stress Cracking of Line Pipe Steels", Corrosion, July, 2003

[13] Koh S., Yang B., Kim K., Yang B., "Effect of Line Pipe Steel Microstructure on Susceptibility to Sulfide Stress Cracking of Line Pipe Steels", Corrosion, July, 2003

[14] Jones R. H., Ricker R. E., Metals Handbook, Vol. 13, Corrosion, 9th Edition, ASM International, 1996, p. 145

[15] Staechle R. W., "Stress Corrosion Cracking and Hydrogen Embitterment of Iron Base Alloys", Staechle R. W., et. al. eds., NACE-5, NACE, Houston, 1977, p. 193

[16] M. Pourbaix, Atlas of Electrochemical Equilbria in Aqueous Solutions, Pergamon Press, New York, 1966

[17] Parkins R. N., "The Controlling Parameters in Stress Corrosion Cracking", 5th Symp, Line Pipe Research, American Gas Association, Arlington, VA, 1974

[18] David G. E., Technical Report 33, Solarton Instruments, Hampshire, Issue 2, 1997

[19] Jones D., Principles and Prevention of Corrosion, 2nd Edition, Prentice-Hall, NJ, 1996

[20] Ferreira M.SG.S, Simoes, A.M.P,"Electrochemical and Optical Techniques for the Study and Monitoring of Metallic Corrosion", Academic Publishers, Netherlands, 1991, p. 485.

[21] Strehblow H. H., in International Congress on Metallic Corrosion, Toronto, NRC, Ottawa, Canada, 1984, Vol, 2, p. 99

[22] R. Winston Revie, Uhlig's Corrosion Handbook, Chapter 10, John Wiley & Sons, Inc., 2nd Edition, 2000

[23] R. C. Newman, in: A. Turnbull (Ed.), Corrosion Chemistry within Pits, Crevices and Cracks, HMSO, London, 1987, p. 14

[24] J. R. Galvele, Journal of Electrochemical Society, 123 (1976) 464

[25] T. P. Hoar, W. R. Jacob, Nature 216 (1967) 1209

[26] G. T. Burstein, P.C. Pistrius, S.P. Mattin, Corrosion Science 35 (1993) 57

[27] Z. Szklarska-Smialowska, Pitting Corrosion of Metals, NACE, Houston, TX, 1986, P. 201

[28] S. Simard, H. Menard, L. Brossard, Journal of Applied Electrochemistry, 28 (1998) 151

[29] A. J. Sedriks, Corrosion of Stailess Steels, John Wiley & Sons, New York, 1978

[30] Z. Szklarska-Smialowska, M. Janik-Czachor, "The Analysis of Electrochemical Methods for Determination of Characteristic Potentials of Pitting Corrosion", Localized Corrosion, NACE-3, R. Staehle, B. Brown, J. Krunger, A. Agrawal, Eds., National Association of Corrosion Engineers, Houston, TX, 1974, P. 353

[31] Z. Szklarska-Smialowska, Proc. Int. Symp. Sulfide Inclusions in Steel, Port Chester, New York, American Society of Metals, Metals Park, Ohio, 1974

[32] M. B. Ives, S.C. Srivastava, in: H. Isaacs, U. Bertocci, J. Kruger, S. Smialowska (Eds.), Advances in Localized Corrosion, NACE, 1990, p. 295

[33] C. S. Brossia, R. G. Kelly, in: P. M. Natishan, R. G. Kelly, G. S. Frankel, R. C. Newman (Eds.), Critical Factors in Localized Corrosion II, the Electrochemical Society, 1995, p. 201, ,PV 95-15

[34] R. C. Alkire, in: P. M. Natishan, H. S. Isaacs, M. Janic, V. A. Macagno, P. Marcus, M. Seo (Eds.), Passivity and its Breakdown, the Electrochemical Society, 1998, p. 34, PV 97-26

[35] J. E. Castle, R. Ke, Corros. Sci. 30 (1990) 409

[36] R. Kiessling, Proc. Int. Symp. Sulfide Inclusions in Steel, Port Chester, New York, American Society of Metals, Metals Park, Ohio, 1974

[37] G. S. Eklund, J. Electochem., Vol. 121, p. 467 (1974)

[38] M. A. Baker and J. E. Castle, Corros. Sci. 34 (1993) 667

[39] R. N. Parkins, C. S. O'Dell and R.R. Fessler, Corros. Sci. 32 (1984) 343-374

[40] E. B. Castro, J. R. Vilche and A.J. Arvia, Corros. Sci. 24 (1991) 37

[41] M. Odziemkowski, J. Flis and D. E. Irish, Electrochem, Acta 39 (1994) 2225

[42] J. M. Blengino, M. Keddam, J. P. Kabbe and L. Robbiola, Corros. Sci. 37 (1995) 621

[43] M. Abdelmoula, Ph. Refait, and J. M. Genin, Corros. Sci. 38 (1996) 623

[44] W. Chen et. al., "Microstructure Dependence of SCC Initiation in X-65 Pipeline Steel Exposed to a Near-Neutral pH Soil Environment", Corrosion, Vol. 60, 2002

[45] J. Park et. al., "Effect of Passivity of the Oxide Film on Low pH SCC of API 5L X-65 Pipeline Steel in Bicarbonate Solution", Corrosion, Vol. 58, 2001

[46] R. N. Parkins, Proc. of the 1st International Conf. on Environmental Induced Cracking of Metals, Kohler, WI, 1988, p. 1-19

[47] R. N. Parkins, Parkins Symposium on fundamental Aspects of SCC, Cincinnati, OH, 1991, P. 3-40

[48] E. Dayalan, G. Vani, J.R. Shadley, S. A. Shirazi, E. F. Rybicki, Corrosion/95, Paper no. 118. NACE International (1995)

[49] G. I. Ogundele, W. E. McMurdie, B. S. Simpson, J. Am. Ceram. Soc. 39 (5) (1956) 168

[50] Lide DR, editor. 79th ed. Handbook of chemistry and physics. Boca Raton: CRS Press, 1998-1999

[51] Dugtad A., Hemmer H., Seresten M., "Effect of Steel Microstructure upon Corrosion Rate and Protective Iron Carbonate Film Formation", Corrosion, Paper # 24, Houston, TX: NACE International, 2000

[52] Mora-Mendoza JL, Turgoose S., "Fe_3C Influence on the Corrosion Rate of Mild Steel in Aqueous CO_2 Systems under Turbulent Flow Conditions". Corros Sci 2002; 44: 1223-1246

[53] Crolet JL, Thevenot N, Nesic S. "The Role of Conductive Corrosion Products in the Protectiveness of the Corrosion Layers", Corrosion 1998; 54: 194-203

[54] Stegmann DW, Hausler RH, Cruz CI, Sutanto H, "Laboratory Studies on Flow Induced Localized Corrosion in CO_2/H_2S environments", PartI: Development of Test Methodology. Corrosion, Paper # 5, Houston, TX: NACE International, 1990

[55] Ueda M, Takabe H, "Effect of Environmental Factor and Microstructure on Morphology of Corrosion Products in CO_2 Environments", Corrosion, Paper # 13, Houston, TX: NACE International, 1999

[56] N. Cui, L. J. Qiao, J. L. Luo, S. Chiovelli, " Pitting of Carbon Steel with Banded Microstructure in Chloride Solutions", British Corrosion J. 2000, Vol. 35, No. 3

[57] Niece PI, Ueda M, "The Effect of Microstructure and Chromium alloying Content on the Corrosion Resistance of Low Alloy Steel Well Tubing in Seawater Injection Service", Corrosion, Paper # 3, Houston, TX: NACE International, 1998

[58] Lopez DA, Schriner WH, De Sanchez SR, Simison SN, " the influence of carbon steel microstructure on corrosion layers, XPS and SEM Characterization", Appl Surf Sci 2003; 207(1-4):69-85

[59] Niece PI, Takade H, Ueda M, "The Development and Implementation of a new Alloyed steel for Oil and Gas Production Wells", Corrosion, Paper # 154, Houston, TX: NACE International, 2000

[60] Kermani MB, Dougan M, "Development of Low Carbon Cr-Mo Steels with Exceptional Corrosion Resistance for Oilfield Applications", Corrosion, Paper # 1065, Houston, TX: NACE International, 2001

[61] Heuer JK, Stubbings LF, "An XPS Characterization of $FeCO_3$ Flms from CO_2 Corrosion", Corros Sci 1999; 41: 1231-1243

[62] de Waard C, Lotz U, Milliams DE, "Predictive Model for CO_2 Corrosion Engineering in Wt Ntural Gs Ppelines", Corrosion 1991; 47(12): 976-985

[63] Nesic S, Lunde L, "CO_2 Corrosion of Carbon Steel in Two-Phase Flow", Corrosion 1994 50(9): 717-727

[64] Murata T, Sato E, Matsuhashani R, Houston, TX: NACE International, 1985, p. 64-71

[65] L. Meyer Paper, Proceedings of the International Symposium Niobium 2001, (Orlando, Florida, USA), Refrences 1 & 2

[66] P. A. Peters and H. G. Hillendbrand, "Experience in Supply of Arctic Grdae Line Pipe for Soviet Construction Projects", World Materials Congress 1988, Chicago, USA, 1988

[67] W. F. Smith, "Structure and Properties of Engineering Alloys", McGraw-Hill Inc, 2nd edition, 1993

[68] H. G. Hillendbrand, and P. Schwaab, "Determination of the Microstructure of High Strength Structural Steels for Correlation with their Mechanical Properties", Mat. Sci. Eng., 94 (1987)

[69] P. A. Peters et al., "Modern Line Pipe Steels for Offshore Use", Offshore Pipeline Technology Seminar, Stavanger, Norway, 1988

[70] K. Hulka, F. Heisterkamp and B. Jones, "HSLA Steels Metallurgy and Applications", ASM International, 1986, 475-484

[71] H. G. Hillendbrand et. al., "Development of Large-Diameter Pipe in Grade X100", Pipeline Technology Conference, Brugge, Belgium 2000

[72] A. J. Davenport, L. J. Oblosky, M. P. Ryan, M. F. Tney, J. Electrochem. Soc. 147 (2000) 2162

[73] N. E. Hakiki, M. de Cunha Belo, A. M. P. Simoes, M. G. S. Ferreira, J. Electrochem. Soc. 145 (1998) 3821

[74] F. Beck, R. Kaus, M. Oberst, Electrochem. Acta 145 (1995) 173

[75] M. M. El-Naggar, J. Appl. Electrochem. 34 (2004) 911

[76] D. H. Davies, G. T. Burstein, Corrosion 36 (1980) 416

[77] K. Videm, A. M. Koren, Corrosion 49 (1993) 746

[78] J. Jelinek, P. Newfeld, Corros. Sci. 20 (1980) 489

[79] [25] Z. Szklarska-Smialowska, Pitting Corrosion of Metals, NACE, Houston, TX, 1986, P. 204 and 347

[80] J. H. Wang, G. C. Su, Z. Szklarska-Smialowska,, Corros. Sci. 44 (1988): p. 732

[81] J. D. Kim, S. I. Pyun, Corros. Sci. 38 (1996): p. 1093

[82] B. Chexal, B. Dooley, Flow-Accelerated Corrosion in Power Plants, 2nd ed., EPRI, CA, 1996, p. 3-93

[83] D. V. Edmonds and R.C. Cochrane, "The Design of X-80 to X-120 Steels with Increased Carbonic Acid Corrosion Resistance", Institute for Materials Research, University of Leeds, Leeds, UK

[84] D. V. Edmonds and R.C. Cochrane, "The Effect of Alloying of Carbon Steel for Oilfield Applications to CO_2 Corrosion", Materials Research. Vol. 8, No. 4, 377-385, 2005

[85] R. E. Mechres, "Effect of Alloying on Maximum Depth of Pits in Mild Steel in Marine Immersion Environments", Corrosion, Vol. 61, No. 4, 2004

[86] T. Nishimura, H. Katayama, K. Noda, T. Kodama, Corros. Sci. 44 (1988): p. 732

[87] K. Ogura, T. Ohama, Corrosion 40 (1984) 47

[88] D. A. Stout, J. B. Lumsden, R. W. Staehle, Corrosion 35 (1979) 141

[89] R. C. Newman, Corros. Sci. 25 (1985) 331